SCIENCE CHINA
Earth Sciences

•RESEARCH PAPER•

September 2018 Vol.61 No.9: 1238–1260
https://doi.org/10.1007/s11430-017-9201-y

Indication from finite-frequency tomography beneath the North China Craton: The heterogeneity of craton destruction

Xiaobing XU[1], Liang ZHAO[1,2*], Kun WANG[1] & Jianfeng YANG[1]

[1] *State Key Laboratory of Lithospheric Evolution, Institute of Geology and Geophysics, Chinese Academy of Sciences, Beijing 100029, China;*
[2] *Chinese Academy of Sciences Center for Excellence in Tibetan Plateau Earth Sciences, Beijing 100101, China*

Received May 24, 2017; revised March 13, 2018; accepted April 9, 2018; published online July 18, 2018

Abstract We picked new traveltime residual datasets in three frequency bands (0.02–0.1, 0.1–0.8, and 0.8–2.0 Hz) for P-waves from 793 teleseismic events and two frequency bands (0.02–0.1 and 0.1–0.8 Hz) for S-waves from 310 teleseismic events, recorded by 389 permanent stations of the China National Seismic Network and 832 broadband stations of 10 temporary arrays deployed in the North China Craton (NCC) region. The final datasets are composed of 65628 P-arrivals and 47050 S-arrivals. Based on previous research and our team's 2012 tomographic work, we constructed new three-dimensional P-velocity and S-velocity models of the NCC through some improvements, such as augmenting a much denser station coverage in the western NCC, considering the incident angle effect in crustal correction and using a multi-frequency joint inversion tomographic technique. The new velocity models provide several salient features, from which we draw possible inferences on regional dynamic processes. We observed high-velocity anomalies in the mantle transition zone (MTZ). Obvious morphological heterogeneities suggest buckling and/or fragmentation of the subducted Pacific slab, and some of the slab materials are visible below 660-km discontinuities. The velocity structure of the eastern NCC is dominated by small-scale lateral heterogeneities. At shallow depths, high-velocity anomalies beneath the southern part of the eastern NCC and the Yanshan region likely represent a remnant of cratonic lithosphere, which may suggest that the NCC destruction is spatially non-uniform. We also detected a high-velocity anomaly in the Sulu Orogen extending downward to ~300 km, which is seemingly controlled by the Tan-Lu Fault. The northern boundary of this anomaly spatially coincides with the Yantai-Qingdao-Wulian Fault, and is likely a remnant of the Yangtze cratonic lithosphere subducting northwestward. Significant low-velocity anomalies imaged beneath the central NCC show a spatial discordance between their northern and southern parts. The northern low-velocity anomaly extends downward to the top of MTZ with a lateral NW-SE strike, whereas the southern one tapers off at ~200–300 km. Low-velocity anomalies are present beneath the Phanerozoic orogenic belts surrounding the NCC, the Paleoproterozoic Trans-North China Orogen, and the Tan-Lu Fault. This feature not only shows excellent spatial correlation with the orogens at the surface, it also exhibits a consistent vertical continuity in a depth range of 60–250 km. This intriguing feature suggests that the collisional orogenic belts and Tan-Lu Fault are inherited weak zones, which may play a key role in craton destruction. By combining multidisciplinary results in this area, we suggest that the spatial heterogeneities associated with the NCC destruction most likely result from the combined effects of a spatially non-uniform distribution of wet upwellings triggered by the subducted Pacific slab and pre-existing weak zones in the cratonic lithosphere.

Keywords Upper mantle, Mantle transition zone, Finite frequency, Multi-frequency joint inversion, Wet upwellings, Weak zones

Citation: Xu X, Zhao L, Wang K, Yang J. 2018. Indication from finite-frequency tomography beneath the North China Craton: The heterogeneity of craton destruction. Science China Earth Sciences, 61: 1238–1260, https://doi.org/10.1007/s11430-017-9201-y

* Corresponding author (email: zhaoliang@mail.iggcas.ac.cn)

1. Introduction

Cratons are characterized as geological units with high degrees of differentiation, refractory lithospheric mantle, lower density (Wu et al., 2008), relatively thick lithosphere (250–300 km; Polet and Anderson, 1995; Artemieva and Mooney, 2001), and lower heat flow (Davies, 2013). These characteristics are favorable to protecting a craton from destruction and maintaining its long-term stability. However, cratons are not indestructible as was previously thought, and the North China Craton is a typical representative of craton destruction.

The NCC, in the eastern part of the Eurasian Plate, is one of the world's oldest cratons with crustal rock dating back to 3.8 Ga (Liu et al., 1992). The Yanshan and Ordos blocks collided during the Paleoproterozoic, integrating into the Western Block along the Inner Mongolia Suture Zone (Zhao et al., 2003). After this, two major Archean blocks, the Western Block and Eastern Block, amalgamated into the NCC along the Trans-North China Orogen (TNCO), and the NCC finished its final cratonization ~1.85 Ga ago (Zhao et al., 2001, 2003). The NCC is bounded by orogenic belts (Figure 1): the Early Paleozoic Qilianshan Orogen to the west (Pan et al., 2006; Xiao et al., 2009), the Central Asian Orogenic Belt (CAOB)—formed by Late Permian-Early Triassic collision with the Siberian Block—to the north (Davis et al., 2001; Xiao et al., 2003), and the Qinling-Dabie-Sulu Orogen (QL-DB-SL Orogen)—derived from a Triassic collision with the Yangtze Craton—to the south and east (Li et al., 1993; Zhao et al., 2001). Along the eastern boundary of the NCC is the Tan-Lu Fault (TLF), a strike-slip fault that extends thousands of kilometers and has its origin and development closely related to the Mesozoic continental collision between the NCC and the Yangtze Craton (Yin and Nie, 1996; Zhang, 1997; Zhu G et al., 2009). Although it has experienced multiple tectonic event stages, the NCC was stable from its formation to the Early Mesozoic (Zhao Y et al., 2010).

The NCC has gone through tectonic reactivations since the mid-Mesozoic, with the ~200 km lithosphere of the eastern NCC having been significantly reduced to ~80 km and changes of craton properties. The presence of such geological phenomena is a characteristic of craton destruction (Griffin et al., 1998; Chen et al., 2008; Zheng et al., 2008; Zhu and Zheng, 2009; Zhu R X et al., 2012b). Multidisciplinary evidence shows that, the dominant driving force of the NCC destruction was sustained subduction of the western Pacific plate (Zhu R X et al., 2012b). However, the specific NCC destruction mechanism is still under debate (Wu et al., 2008, 2014). Some hypotheses have been proposed, such as lithospheric delamination (Deng et al., 1994; Gao et al., 2004), thermal-chemical erosion (Xu, 2001; Xu et al., 2008) and peridotite-melt interaction (Zhang, 2009) among others.

Deep mantle processes are thought to possibly cause near-surface geologic responses. Some examples are subduction-induced mantle upwelling, which has been invoked to explain intracontinental volcanism (Zhao et al., 2004; Lei et al., 2013); slab roll-back, which may have helped form extensional basins and fault systems (Zhu G et al., 2012); and continental subduction, which has been considered a cause of high-pressure and ultrahigh-pressure metamorphic rock zones (Guillot et al., 2009; Zhao L et al., 2017). To better understand the origins and effects of deep mantle processes, we need to obtain high-resolution three-dimensional (3-D) data on Earth's interior structure, and seismic tomography has been proven to be a powerful tool for probing structures of the crustal and mantle. Our purpose in this paper is to obtain high-resolution 3-D P- and S-velocity models of the mantle beneath the NCC, with the aim of furthering knowledge of the dynamic upper mantle processes in this area.

Recent years have seen many traveltime tomography studies of the NCC, with some imaging models focusing on the origins and effects of large-scale anomalies (e.g., Lebedev and Nolet, 2003; Huang and Zhao, 2006; Li et al., 2006, 2008; Feng et al., 2010; Li and van der Hilst, 2010; Obrebski et al., 2012; Zhao et al., 2012; Chen et al., 2015). For instance, Lebedev and Nolet (2003) demonstrated an S-wave model with horizontal resolution no better than 500 km because of the traditional surface-wave tomography method and relatively low-frequency data they used. With constraints of S- and surface-wave data, Obrebski et al. (2012) obtained an S-wave model with a horizontal resolution in the range of 3°–4.5°. The highest resolution in the models of Li (Li et al., 2006, 2008; Li and van der Hilst, 2010), was ~300 km, whereas the model of Feng et al. (2010) showed a horizontal resolution ranging from 2° in the shallow regions to 4° in deep regions. In addition, the model of Zhao et al. (2012) presented a ≥200 km resolution. Some other imaging models focused on specific research areas, such as the Sulu orogenic belt (Xu et al., 2002) and crust under Beijing and surrounding regions (Huang and Zhao, 2004; Lei et al., 2008). Sun et al. (2006, 2008a, 2008b) obtained velocity models of the crust and uppermost mantle, which showed a good agreement with surface geologic structure. However, the link between shallow structures and deep mantle processes is not clear.

Our approach differed from studies of the NCC using the ray-theoretical tomography method of Zhao et al. (1994) (e.g., Huang and Zhao, 2006; Tian et al., 2009, 2011; Xu and Zhao, 2009; Lei, 2012), in that we preferred to use finite-frequency seismic tomography (Dahlen et al., 2000; Hung et al., 2000) to study the entire NCC (100°–124°E, 26°–46°N). We made some improvements to enhance resolution to our team's 2012 work (Zhao et al., 2012). We improved the

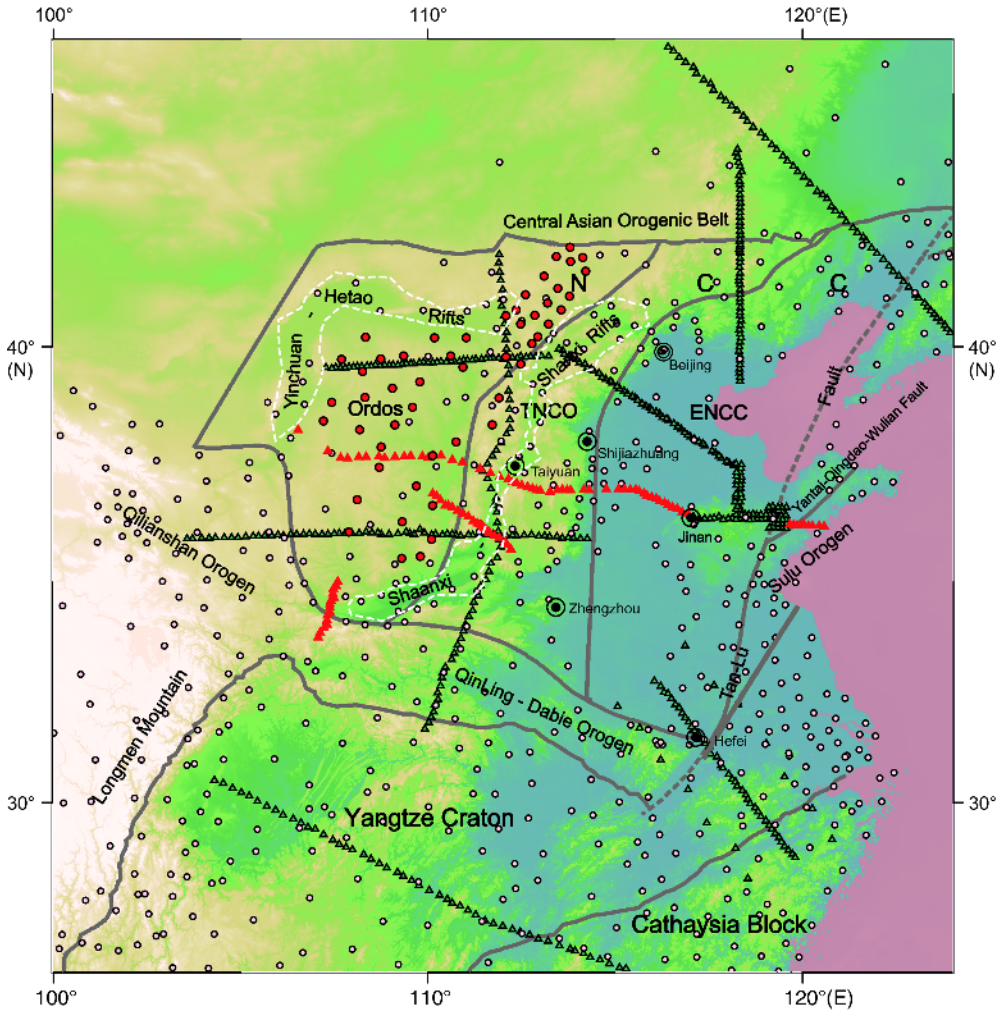

Figure 1 Regional map showing major tectonic features and seismic stations used in this study. Gray solid lines demarcate the major tectonic provinces. Gray dashed lines mark the Tan-Lu Fault. White dashed lines mark the Cenozoic rift systems. Pink circles mark the permanent stations of the China National Seismic Network (CNSN). Green triangles mark the temporary seismic arrays NCISP1–NCISP8, deployed by the Institute of Geology and Geophysics, Chinese Academy of Sciences (IGG, CAS). Red triangles mark the temporary seismic array deployed by Peking University. Red circles mark the temporary seismic array deployed by the Institute of Geophysics, China Earthquake Administration. NCC: North China Craton; TNCO: Trans-North China Orogen; ENCC: eastern North China Craton.

seismic ray coverage of the western NCC by adding two temporary arrays. Additionally, we applied a multi-frequency joint inversion tomographic technique with picking seismic data in different frequency bands and took incident angle into account when conducting crustal correction. As indicated by resolution tests, our new velocity models have a higher spatial resolution. In addition, they are consistent with previous studies of global features, and reveal the spatial heterogeneity of the NCC destruction and importance of pre-existing weak zones in craton destruction.

2. Data and method

2.1 Research area and seismic observation

In this paper we used data recorded by several seismic arrays deployed in the research area (100°–120°E, 26°–46°N), including the dataset our team using in their 2012 tomography work. One part of the data is from the North China Interior Structure Project, including profiles NCISP1–NCISP8, which included readings from a total of 681 stations and operated from 2000 to 2011 (green triangle in Figure 1). The other part is from the China National Seismic Network, which used 389 evenly distributed stations and made observations from 2007 to 2012 (pink circles in Figure 1; Zheng et al., 2010). We combined new datasets from two temporary arrays, one 100-station array deployed by Peking University from 2005 to 2010 (red triangle in Figure 1) and another 51-station array operated by Institute of Geophysics, China Earthquake Administration deployed mainly in the western NCC in 2010 and 2011 (red circle in Figure 1). These four datasets yield much denser ray coverage of the western NCC and North China Basin than previous studies.

2.2 Data picking and analysis

To conduct teleseismic tomography, we used events that were recorded by at least 10 stations from epicentral distances of 25°–98°. To ensure the spatial uniformity of each source-station pair, we removed events with duplicate locations. The ultimate dataset consisted of 310 P-wave seismic events (Appendix Figure S1a, http://link.springer.com) and 793 S-wave seismic events (Appendix Figure S1b). Traveltime delays are frequency-dependent because of wave diffraction and wavefront healing (Appendix Figure S2a; Hung et al., 2004; Zhao et al., 2016). To take advantage of this feature, we measured relative traveltime residuals in multiple frequency bands (0.02–0.1, 0.1–0.8, and 0.8–2.0 Hz for P-wave events, and 0.02–0.1 and 0.1–0.8 Hz for S-wave events) using a multichannel cross-correlation technique (Van Decar and Crosson, 1990) on the basis of IASP91 model (Kennett and Engdahl, 1991) assumption. Compared to automatic picking methods (e.g., Chevrot et al., 2014), our picking method effectively avoids cycle skipping and enhances picking accuracy because of interactive confirmation. To ensure the reliability of the traveltime residuals picked, we discarded data that completely deviated from the reference trend of the P- and S-wave relative traveltime residual ratio with common stations and events (Appendix Figure S3a). We finally used 65628 P-arrivals with a deviation of 0.004 s and 47050 S-arrivals with a deviation of 0.012 s in our inversions (Table 1). Lateral P- and S-wave speed variations are indicated by azimuthally averaged traveltime residuals at each station (Appendix Figure S3b–d). These traveltime residuals also foreshadow first-order features of our final inversion model. The Ordos Bock shows negative traveltime residuals (early arrivals), whereas the northern part of the central NCC shows positive traveltime residuals (late arrivals). The traveltime residuals of both areas do not display an azimuthal correlation.

2.3 Method

We used finite-frequency seismic tomography (Dahlen et al., 2000; Hung et al., 2000; Hung et al., 2004; Ren and Shen, 2008; Liang et al., 2011) to invert P- and S-wave structures beneath the NCC. We calculated the Fréchet travel time sensitivity kernels based on the IASP91 one-dimensional layered model, which is superior to conventional ray-theoretical methods, and this banana-doughnut theory accounts for wavefront healing, scattering, and other diffraction phenomena. The travel time shift is sensitive to perturbations of 3-D wave speed off the ray path (Dahlen et al., 2000):

$$\delta t = \iiint_{\oplus} \mathbf{K}(\mathbf{x})\delta c(\mathbf{x})/c(\mathbf{x})\mathrm{d}^3\mathbf{x}, \tag{1}$$

where **K** is the 3-D Fréchet sensitivity kernel for a travel time shift δt and $\delta c(\mathbf{x})/c(\mathbf{x})$ is the wave speed perturbation to be imaged. Under an assumption of single scattering, the sensitivity kernel can be expressed as (Dahlen et al., 2000):

$$\mathbf{K}=\frac{1}{2\pi c}\left(\frac{R}{c_t R' R''}\right)\frac{\int_0^\infty \omega^3 \left|\mathrm{s}_{\mathrm{syn}}(\omega)\right|^2 \sin(\omega\Delta T)\mathrm{d}\omega}{\int_0^\infty \omega^2 \left|\mathrm{s}_{\mathrm{syn}}(\omega)\right|^2 \mathrm{d}\omega}, \tag{2}$$

where ΔT represents the additional travel time for the path with a detour through a scatterer between the source and receiver relative to the corresponding direct path. R, R', and R'' are the geometrical spreading factors for the unperturbed ray, the forward source-to-scatterer ray, and the backward receiver-to-scatterer ray, respectively. $\left|\mathrm{s}_{\mathrm{syn}}\right|^2$ is the power spectrum of the synthetic pulse, which shows frequency dependence of the cross-correlated differential travel times. As shown in Section 2.2, measurements of delays of the same phase arrival are frequency-dependence on filtering, which results from differences in spatial sampling of the velocity structure off the ray path for sensitivity kernel **K** at different frequencies. Thus, the measured delays of each source-station pair at different frequencies provide additional spatial sampling information.

We parameterized the image volume with a regular 64×64×64 grid that was centered at 112°E, 36°N. The grid has a cell spacing of ~42 km in longitude, ~35 km in latitude, and ~23 km in depth. After parameterization, we can express the travel time equations as a discrete form:

$$\mathbf{d}_i=\mathbf{G}_{ij}\mathbf{m}_j, \tag{3}$$

where $\mathbf{d}_i$ is the ith measured relative travel time shift, $\mathbf{G}_{ij}$ is the differential value of the integrated volumetric kernels of the ith event contributing to the jth node, and $\mathbf{m}_j$ is the model parameter at jth node. The standard damped least square solution (Paige and Saunders, 1982; Nolet, 1985) of this inversion problem is:

$$\widehat{\mathbf{m}}=(\mathbf{G}^{\mathrm{T}}\mathbf{G}+\theta^2\mathbf{I})^{-1}\mathbf{G}^{\mathrm{T}}\mathbf{d}, \tag{4}$$

where **I** is the identity matrix and θ is the optimal inversion damping factor, which is determined by considering the trade-off between the variance reduction and model norm, as shown in Figure 2. To suppress poorly constrained small-scale variations, we also applied a smoothness regularization scheme involving convolutional quelling to matrix **G** (Meyerholtz et al., 1989; Hung et al., 2004). Eq. (4) can thus be rewritten as:

$$\widehat{\mathbf{m}}=\mathbf{W}(\mathbf{W}^{\mathrm{T}}\mathbf{G}^{\mathrm{T}}\mathbf{G}\mathbf{W}+\theta^2\mathbf{I})^{-1}\mathbf{W}^{\mathrm{T}}\mathbf{G}^{\mathrm{T}}\mathbf{d}, \tag{5}$$

where **W** is the convolution operator and preferential correlation lengths for the horizontal and vertical directions are twice the size of the cell spacing in this study. We constructed the P- and S-wave models discussed in this paper using a damping factor of 40.0 for P-waves and 50.0 for S-waves, with a variance reduction of ~73% and ~71% for P-waves and S-waves, respectively (shown in Figure 2 as blue circles

Table1 Information of relative traveltime residual datasets[a)]

Phase	Parameters of traveltime dataset	0.02–0.1 Hz Frequency band	0.1–0.8 Hz Frequency band	0.8–2.0 Hz Frequency band	Summation
P-wave (Cross-correlation coefficient >0.85) 310 seismic events	Number of arrivals	19681	28755	17192	65628
	Cross-correlation coefficient	0.97	0.93	0.92	0.94
	RMS error (s)	0.0062	0.00036	0.0029	0.004
S-wave (Cross-correlation coefficient >0.85) 793 seismic events	Number of arrivals	33875	13175		47050
	Cross-correlation coefficient	0.95	0.91		0.94
	RMS error (s)	0.0092	0.019		0.012

a) Taking into account the computational memory, relative traveltime residuals with number greater than 40 and cross-correlation coefficient larger than 0.85 of each seismic event were selected for P-waves, and for S-waves those with number greater than 10 and cross-correlation coefficient larger than 0.85 were selected. In the table, the cross-correlation coefficient and RMS error are both mean values.

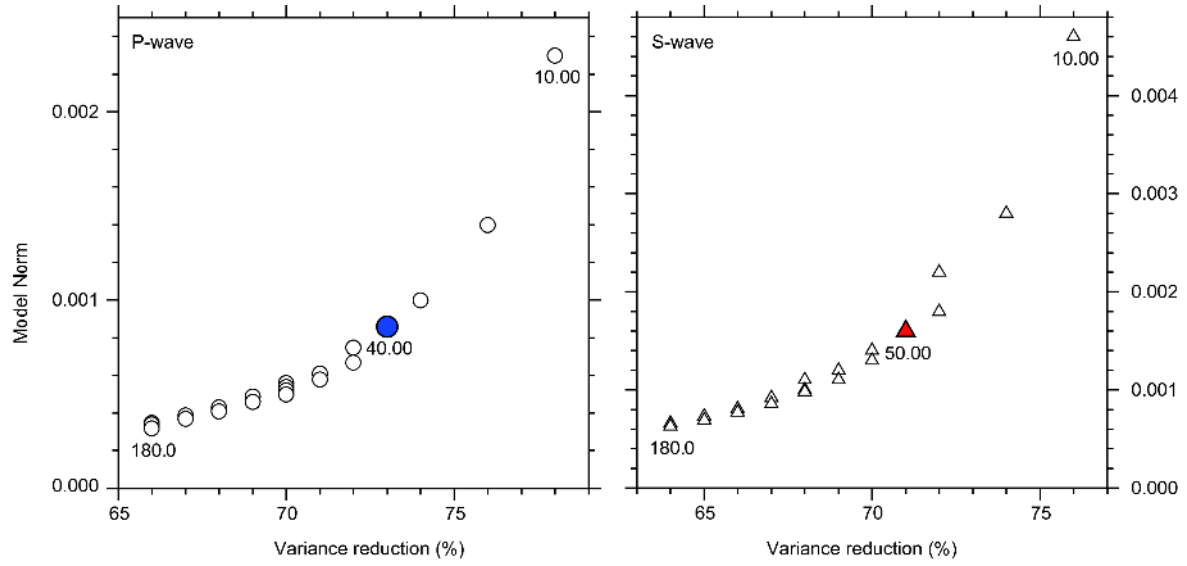

Figure 2 Trade-off curves of model norm and variance reduction for the P- (a) and S-wave (b). The circles and triangles represent the trade-off curves for the P- and S-waves, respectively. The blue circle represents the P-tomographic model shown in Figure 4 with a variance reduction of 73%. The red triangle represents the S-tomographic model shown in Figure 5 with a variance reduction of 71%.

for P-waves, and red triangles for S-waves).

2.4 Crustal correction

Affected by low-velocity crustal sediments, the ray paths of teleseismic body waves are nearly vertical and rarely cross each other at shallow depths. The crust is therefore poorly constrained, yielding a lower resolution. Contamination of upper mantle tomography by crustal travel time anomalies is a phenomenon known as smearing effect, which is obvious in areas with sparsely distributed stations. Eliminating crustal heterogeneity effects on traveltime residuals can significantly enhance the quality and reliability of upper mantle imaging results, especially in regions with complex crustal wave speed structures (Ekström and Dziewonski, 1998; Allen et al., 2002; Li et al., 2006; Koulakov et al., 2009). We carried out two common approaches for this correction. In the first approach, we subtracted the calculated crustal traveltime anomalies (Figure 3) from observed travel time residuals based on a regional crustal velocity model (Sun et al., 2008a). The model of Sun et al. (2008a) has a crustal thickness that varies from 30.76 to 61.84 km. Due to the lack of velocity model of uppermost mantle, the selected crustal correction depth is 30.76 km. In the crustal correction, the incident angles of ray paths were calculated according to the IASP91 model. Then, ray paths were traced from the surface to the correction depth layer by layer in the basis of the model of Sun et al. (2008a) and crustal traveltime anomalies were accumulated simultaneously. Therefore, our crustal correction is thus more accurate than our team's 2012 work. In the second approach, we involved station terms and event terms in the inversion. Station terms are aimed at absorbing as much of the delay signature from shallow heterogeneity as possible (Hung et al., 2004), and event terms are intended to

account for baseline shifts between the relative traveltime sets of different events (Allen et al., 2002). By comparing imaging results with and without crustal correction (Appendix Figures S4 and S5, respectively), we can see that the crustal smearing effect on the final model is mainly confined to a depth of 60 km with only small effects deeper.

3. Imaging results

The obtained imaging results are velocity perturbation relative to the IASP91 reference model, presented as plan views (Figures 4 and 5) and vertical cross-sections (Figure 6). The P- and S-velocity models displayed in Figures 4–6 are consistent for large-scale anomalies, but exhibit some local differences. Appendix Figures S6 and S7 are maps of ray numbers crossing each grid node for P- and S-waves, respectively. For P- and S-waves, the ray numbers of each node beneath main research area of the NCC are greater than 1500 (ray density higher than 102 rays per 100 km^3). From the supporting information (comparing Appendix Figure S6a–h and a′–h′, Figure S7a–e and a′–e′), P-waves have a broader ray distribution and higher ray density than S-waves. This is because P-waves have a better signal-to-noise ratio than S-waves, and thus have more detectable traveltime residuals. On the other hand, in addition to using traveltime residuals in the same 0.02–0.1 and 0.1–0.8 Hz frequency bands as S-waves, P-waves also used higher frequency-band traveltime residuals of 0.8–2.0 Hz. Hence, the ray spatial sampling differences between P-waves and S-waves, as well as the much narrower Fresnel zone of P-waves due to the use of higher frequency-band traveltime data, are responsible for local differences of the P- and S-velocity models. The P-velocity model has a higher resolution than the S-velocity model (discussed in Section 4.1 below) and presents more refined features.

In this paper, we only discuss the structural features below 60 km because of poor crust constraints in teleseismic body-wave tomography. In comparison with previous imaging models (e.g., studies of larger research area, such as Huang and Zhao, 2006; Li et al., 2006, 2008; Feng et al., 2010; Li and van der Hilst, 2010; Obrebski et al., 2012; Wei et al., 2012; Zhao et al., 2012; Chen et al., 2015; Zhao D P et al., 2017, and studies of similar research areas, such as Zhao et al., 2009; Tian et al., 2009, 2011; Lei, 2012), the most intriguing feature of our P- and S-velocity models is that the high-velocity anomalies H2′ and H2″, which are distributed in the northern and southern portions of the eastern NCC, respectively, are surrounded by low-velocity anomalies beneath the surrounding orogenic belts and the Tan-Lu Fault. Additionally, these low-velocity anomalies have morphologies that show excellent tectonic correlation (Figures 4a–e and 5a–e). We only compare these results with the models of Tian et al. (2009) and Lei (2012), mainly because these two models cover similar study region sizes and have similar resolution scales as our models.

3.1 Upper mantle images beneath the Ordos Block

As was the case in the studies mentioned above, a significant high-velocity anomaly, H1, is observed beneath the Ordos Block, extending downward to ~300 km (Figures 4a–f, 5a–f, 6a–e, a′–e′, h–i, and h′–i′). Benefit from a higher station density of the central and western NCC (denoted by red circles and triangles in Figure 1), our models show a clearer outline of the Ordos Block than those of Tian et al. (2009) and Lei (2012) (Figures 4a–f, 5a–f, 6a–e, h–i, a′–e′, and h′–i′). H1 gradually moves deeper from north to south (Figures 6a–e, a′–e′, i, and i′), and extends downward to ~400 km locally (Figures 6c–d, c′–d′, and i–i′). This phenomenon is also seen in models from Li and van der Hilst (2010) and Obrebski et al. (2012). A high-velocity anomaly, H6, is visible beneath the Alashan Block, whereas a prominent low-velocity anomaly exists beneath the Yinchuan-Hetao Rift, which separates the Ordos and Alanshan blocks (Figures 4a–f, 5a–f, 6b–c, and c′). These features confirm what has already been observed in previous studies (e.g., Tian et al., 2009; Lei, 2012) despite there being some differences in details between our study and previous studies. In the model of Tian et al. (2009), the high-velocity anomaly beneath the Alashan Block is mainly confined to crustal depths (<30 km), whereas H6 in our model extends from 60 down to ~300 km (Figures 4a–f, 5a–f, 6b–c, and b′). However, the model in Lei (2012) showed a low-velocity anomaly beneath the Hetao Rift, and a high-velocity anomaly beneath the Yinchuan Rift. Located adjacent to the southern margin of the Ordos Block is the Qinling orogen, which was formed by the collision of the NCC and the Yangtze Craton. Within 200 km depth below this region, Lei (2012) showed a prominent low-velocity anomaly, while Tian et al. (2009) showed a high-velocity anomaly, the northern margin of which even stretches into the Ordos block. Compared to these two models, our models exhibit a relatively clear boundary of the Ordos the Yangtze blocks, and the northern margin of the Yangtze Craton seems to stretch farther than its identified surface tectonic lines (shown in Li and van der Hilst, 2010; Zhao D P et al., 2017). We detected either a low-velocity anomaly or a weak high-velocity anomaly with an amplitude lower than the Ordos and Yangtze blocks in the upper mantle beneath the Qinling orogeny (Figures 4a–4f, 5a–5f, 6i, and 6i'; Obrebski et al., 2012).

3.2 Upper mantle images beneath the Trans-North China Orogen

Previous studies have revealed that the TNCO is character-

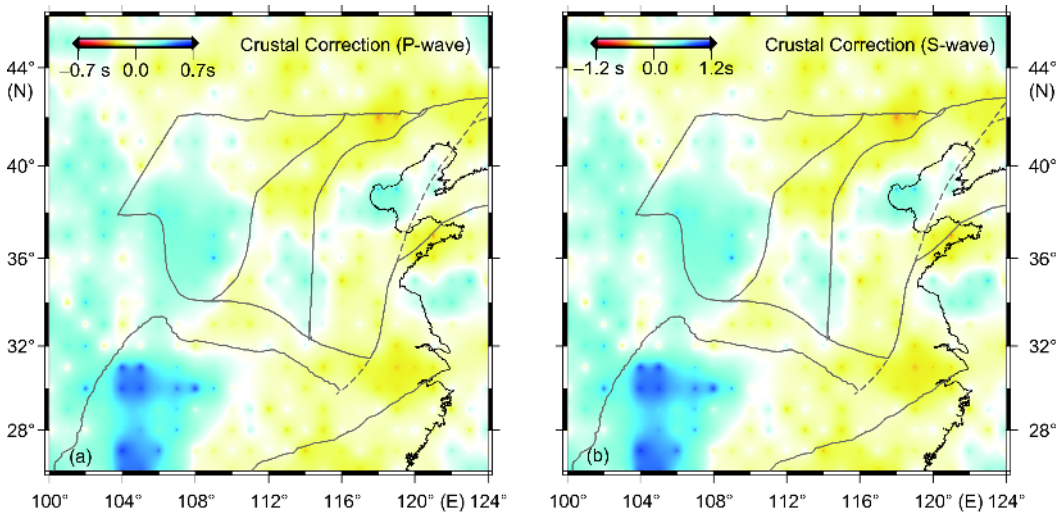

Figure 3 Crustal corrections for the P- (a) and S-wave (b). The reference model used for crustal corrections is the regional S-wave crustal velocity model (Sun et al., 2008a), and corresponding P-wave crustal velocity model was derived based on a Poisson's ratio of 1.765. The crustal correction depths selected are both 37.6 km for the P- and S-waves.

ized as a low-velocity anomaly, extending downward to a depth of ~400 km (e.g., Huang and Zhao, 2006; Li et al., 2006; Tian et al., 2009; Zhao et al., 2009, 2012; Li and van der Hilst, 2010; Lei, 2012; Obrebski et al., 2012; Chen et al., 2015; Zhao D P et al., 2017). This low-velocity anomaly shows a NE-SW orientation in the model of Tian et al. (2009), but in the studies of Lei (2012) and ours it is arc-shaped morphologically (Figures 4a–f and 5a–f). Furthermore, this anomaly in our models appears to be divided into two major low-velocity zones (LVZs), the northern (L1) and southern (L2) parts (Figures 4a–f, 5a–f, 6j, and j′). Two LVZs were also observed in the models of Jiang et al. (2013) obtained from surface wave tomography. L1 stretches northward and southward with a NW-SE strike, and extends downward to the MTZ (Figure 6a–d, g–h, j, e′, and j′). In contrast, L2 shows obvious spatial differences from L1, tapering off at a depth of ~300 km with a small spatial distribution (Figures 4a–f, 5a–f, 6e–f, e′, and j′). In addition to these morphological differences, L1 and L2 also show an amplitude difference. A portion of L1 exhibits a stronger anomaly amplitude of >2% $\delta V_p/V_p$ (P-velocity perturbation) and >3% $\delta V_s/V_s$ (S-velocity perturbation) for P- and S-waves, respectively (Figures 4a–f, 5a–f, 6a–c, j, a′–c′, g′, h′, and j′). These high anomaly amplitude regions spatially correspond to the Datong volcano on the surface (Figures 4a–f, 5a–f, 6a, g, a′, and g′). Between these two LVZs located adjacent to the transtensional zone of the Shaanxi-Shanxi Rift (SSR), a high-velocity anomaly is visible between 60 and 300 km depth, which is connected to the Ordos Block to its west morphologically (Figures 4a–f, 5a–f, 6j, and j′). Tian et al. (2009) and Lei (2012) found the same features in their body-wave models, whereas the surface wave tomographic results of Jiang et al. (2013) showed that this high-velocity anomaly extends to a depth of ~100 km and separated from the Ordos Block by a narrow LVZ (Jiang et al., 2013).

3.3 Upper mantle images beneath the eastern NCC

In contrast to the imaging features in the Ordos Block and the TNCO, the upper mantle of the eastern NCC is dominated by small-scale lateral heterogeneities. Unlike previous studies, one new observational feature in our models is that a prominent low-velocity anomaly, L4, is present within 300 km depth beneath the CAOB, and its strike changes from E-W within 200 km depth to NE-SW in the 200–300 km depth range (Figures 4a–f, 5a–f, 6h, and h′). On the northern side of L4, a southwestward leaning high-velocity anomaly H4 is detected under the region between the Yanshan Block and the Songliao Basin, extending downward to ~350 km (Figures 4a–f, 5a–f, 6h, and h′). This feature is consistent with the results from Lebedev and Nolet (2003), Li et al. (2006) and Tian et al. (2009) in the same area. H4 may represent a Proterozoic mantle terrane beneath the Songliao Basin that extends beyond the present boundary of the basin (Zhang M et al., 1998), and L4's strike change between 200 and 300 km depth may be related to this subduction.

A prominent low-velocity anomaly L3 is imaged beneath the Tan-Lu Fault, located to the east of the eastern NCC. The same features were also shown in previous studies (e.g., Huang and Zhao, 2006; Tian et al., 2009; Zhao et al., 2009, 2012; Lei, 2012; Obrebski et al., 2012), but imaging depth differences of L3 existed among these models. Tian et al. (2009) imaged a low-velocity anomaly extending downward to ~400 km, whereas this low-velocity anomaly in the models of Zhao et al. (2012) extends to the MTZ. In contrast, our models show that L3 occupies the 200–300 km depth

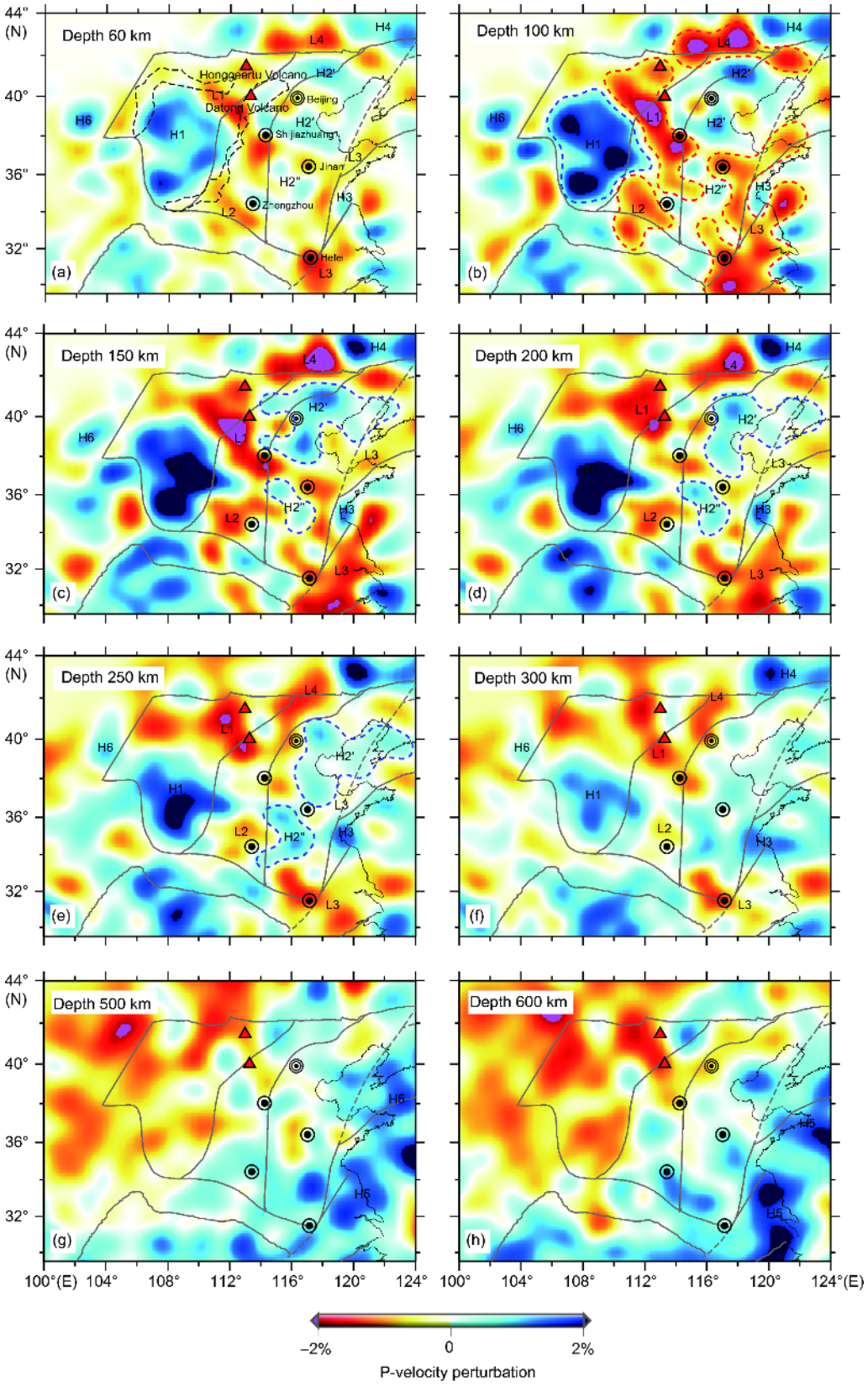

Figure 4 Depth slices of the P-velocity model. The red and blue colors denote the low- and high-velocity anomalies respectively, with corresponding velocity perturbation scale shown on the bottom. Gray solid lines demarcate the major tectonic provinces. Gray dashed lines mark the Tan-Lu Fault. Black dashed lines mark the Cenozoic rift systems surrounding the Ordos Block. Red triangles mark the Datong and Honggeertu volcanoes. L1–L4 represents different low-velocity anomalies, and H1–H5 represents different high-velocity anomalies. Red and blue dashed lines in images (b)–(e) show the outlines of velocity anomalies for geological interpretation.

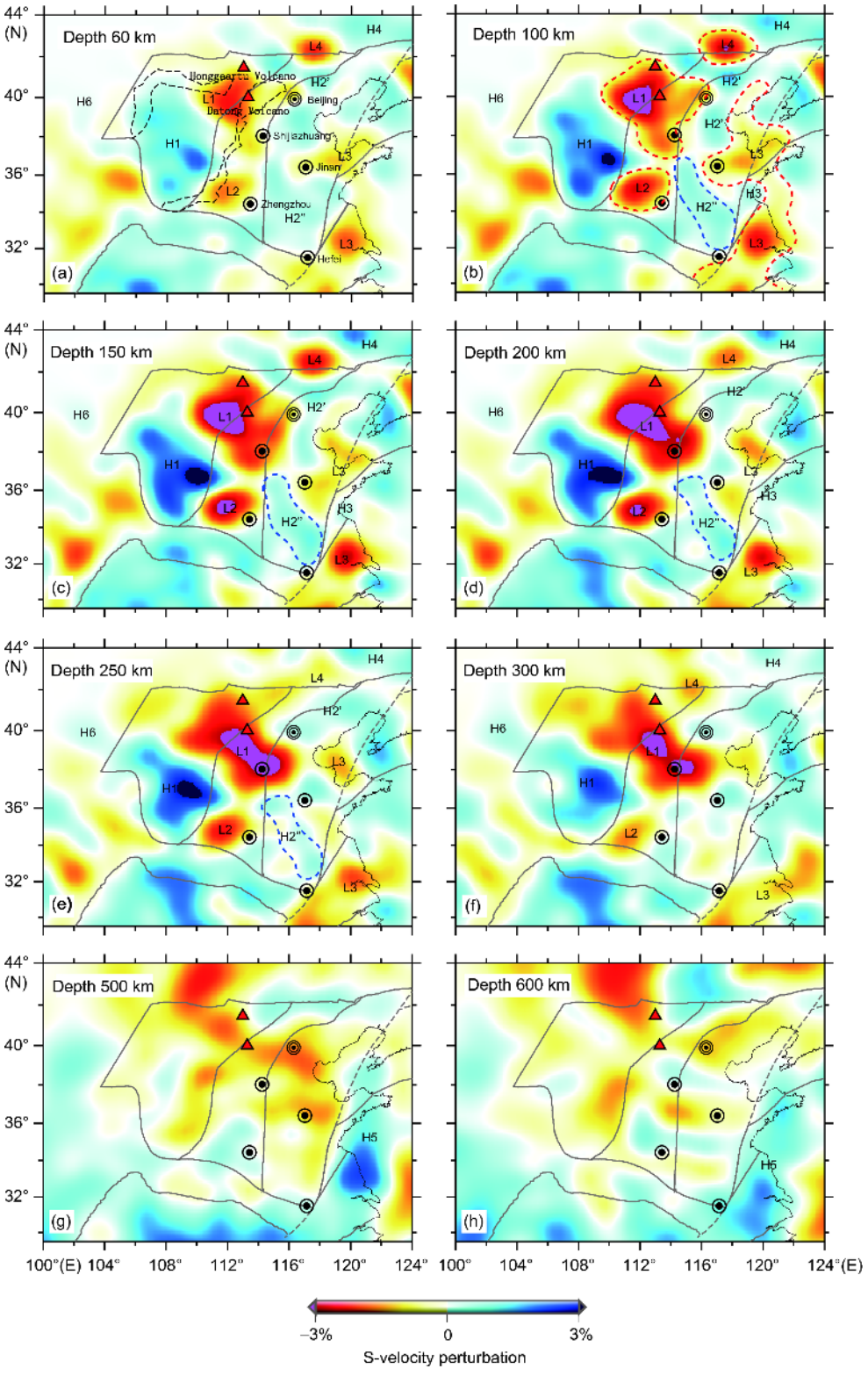

Figure 5 Depth slices of the S-velocity model.

range (Figures 4a–f, 5a–f, 6a–g, k, c′–g′, and k′), which is consistent with studies of Huang and Zhao (2006), Lei (2012) and Obrebski et al. (2012). A remarkable imaging feature in the model of Lei (2012) is that L1 and L3 combine at 200 km depth and extend downward, forming a Y-shaped low-velocity structure. However, as shown in Figure 6g and

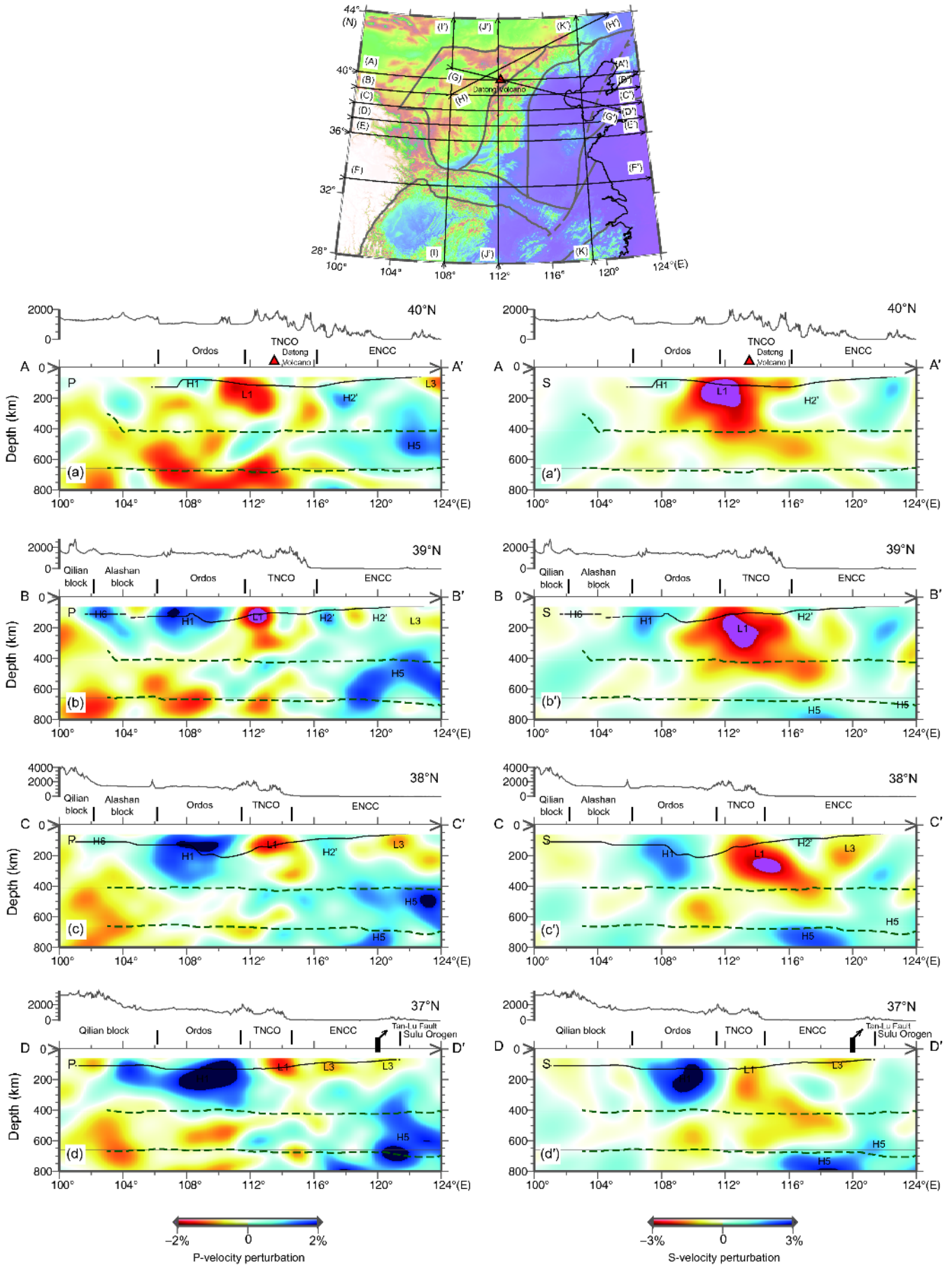
44°(N)
40°
36°
32°
28°
100°
104°
108°
112°
116°
120°
124°(E)
(A)
(B)
(C)
(D)
(E)
(F)
(G)
(H)
(I)
(J)
(K)
(A')
(B')
(C')
(D')
(E')
(F')
(G')
(H')
(I')
(J')
(K')
Datong Volcano
40°N
39°N
38°N
37°N
Qilian block
Alashan block
Ordos
TNCO
ENCC
Tan-Lu Fault
Sulu Orogen
Datong Volcano
Depth (km)
P
S
H1
H2'
H3
H5
H6
L1
L3
(a)
(a')
(b)
(b')
(c)
(c')
(d)
(d')
−2%
0
2%
P-velocity perturbation
−3%
0
3%
S-velocity perturbation

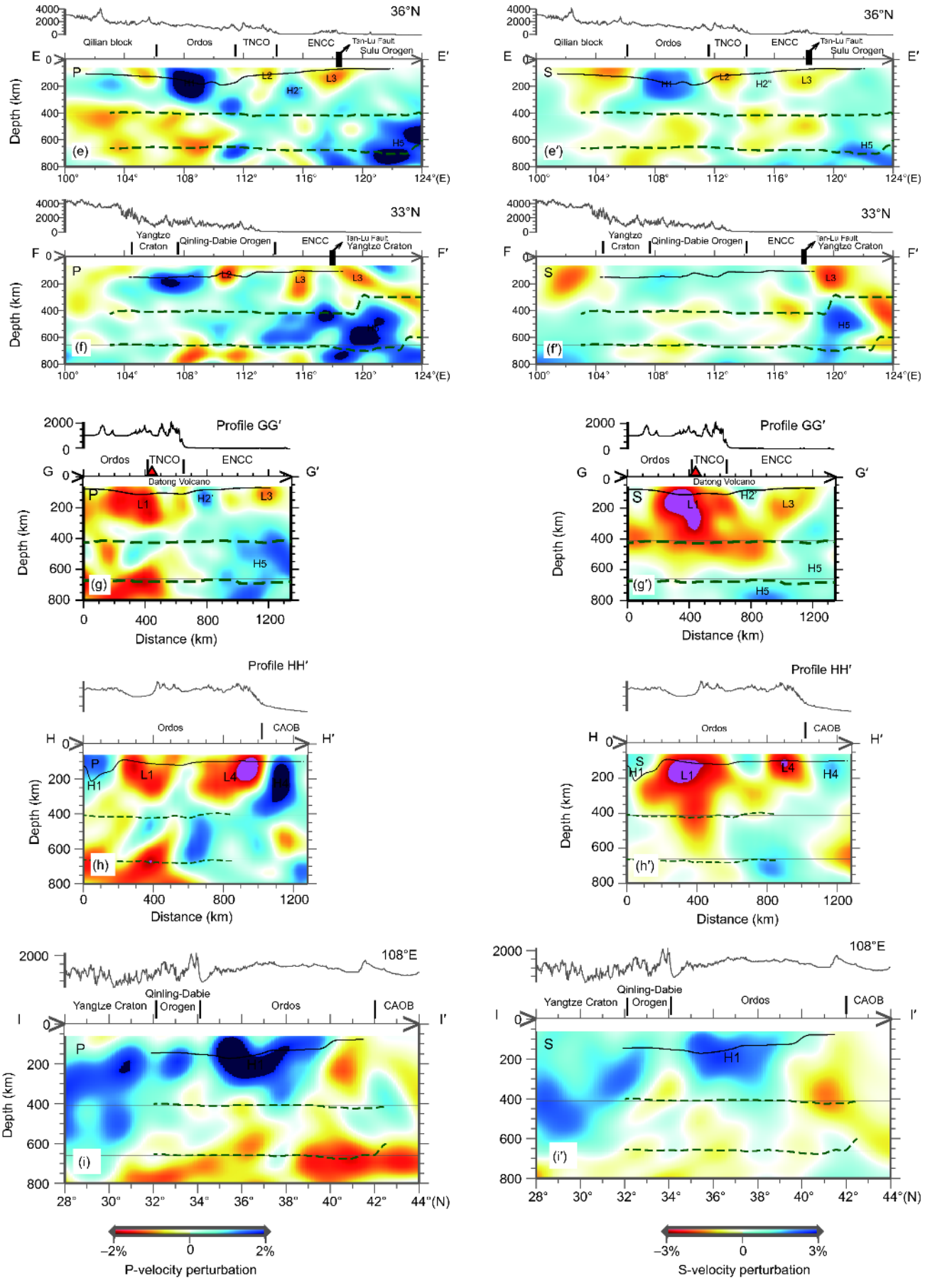
36°N
Qilian block
Ordos
TNCO
ENCC
Tan-Lu Fault
Sulu Orogen
E
E′
P
S
L1
L2
L3
H1
H2′
H2″
H5
(e)
(e′)
Depth (km)
100°
104°
108°
112°
116°
120°
124°(E)
33°N
Yangtze Craton
Qinling-Dabie Orogen
F
F′
(f)
(f′)
Profile GG′
G
G′
Datong Volcano
(g)
(g′)
Distance (km)
Profile HH′
CAOB
H
H′
H4
(h)
(h′)
108°E
Qinling-Dabie Orogen
I
I′
(i)
(i′)
28°
30°
32°
34°
36°
38°
40°
42°
44°(N)
−2%
0
2%
P-velocity perturbation
−3%
3%
S-velocity perturbation

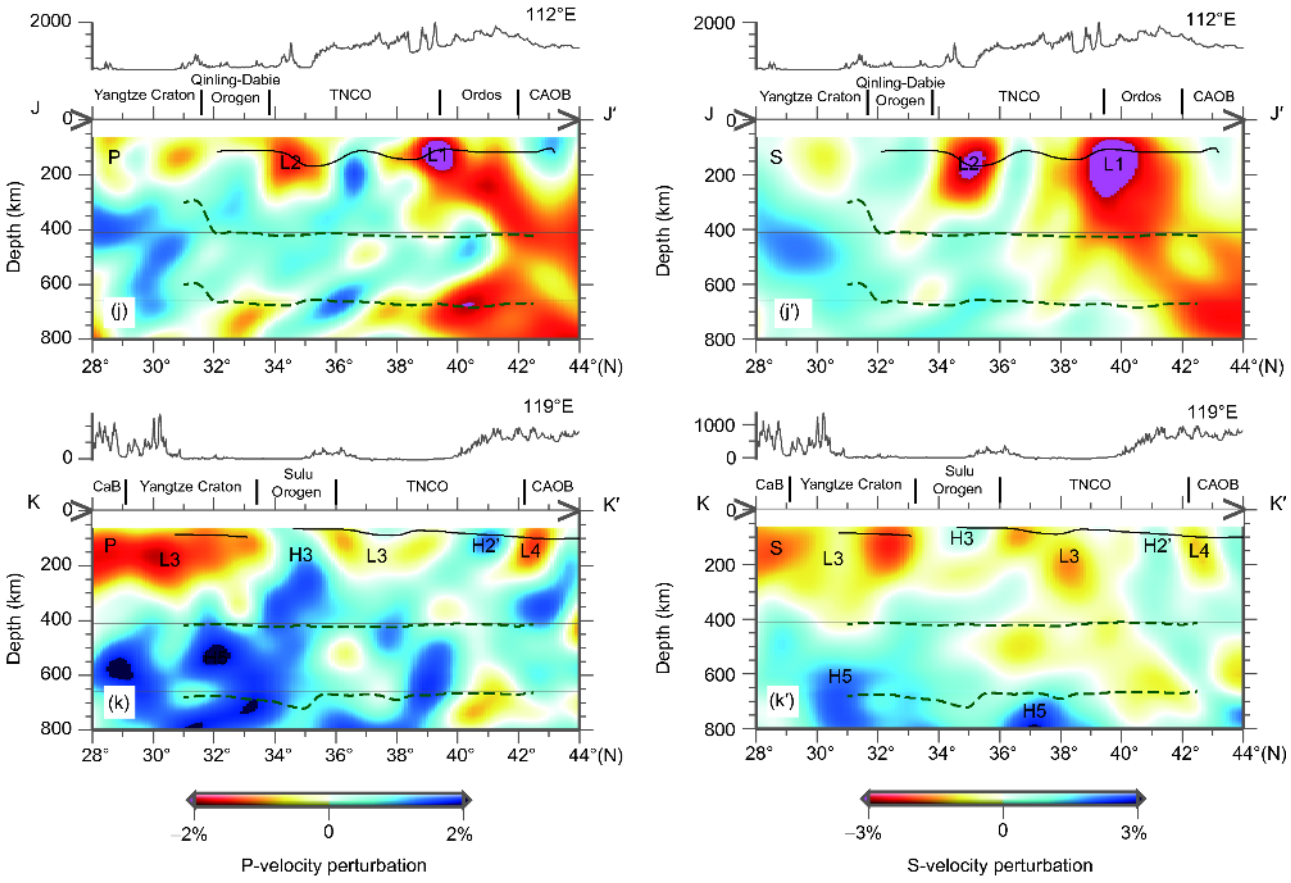

Figure 6 Vertical cross-sections for the P- (left) and S-wave (right). The red and blue colors denote the low- and high-velocity anomalies respectively, with corresponding velocity perturbation scale shown on the bottom. Two gray solid lines mark the 410-km and 660-km discontinuities. Two green dashed lines mark the 410-km and 660-km discontinuities obtained from the receiver function (Zheng et al., 2017). Black solid lines mark the Lithosphere-Asthenosphere Boundary (LAB) obtained from the receiver function (Zheng et al., 2017). L1–L4 represents different low-velocity anomalies, and H1–H5 represents different high-velocity anomalies. CAOB: Central Asian Orogenic Belt; CaB: Cathaysia Block.

g′, our model detected no Y-shaped structure at the same profile position. Instead, L1 and L3 are separated by a high-velocity anomaly H2′, and underlain by a high-velocity anomaly H5.

Surrounded by L1, L2, L3 and L4, H2′ and H2″ are imaged within a depth of 250 km in the Yanshan area and the southern part of the eastern NCC (an area enclosed by Shijiazhuang, Jinan, Hefei, and Zhengzhou), respectively (Figures 4a–e, 5a–e, 6a–c, e, g, k, a′–c′, e′, g′, and k′). Previous models (e.g., Huang and Zhao, 2006; Tian et al., 2009; Zhao et al., 2009, 2012; Li and van der Hilst, 2010; Lei, 2012; Obrebski et al., 2012) also showed high-velocity anomalies beneath the eastern NCC, but exhibited some differences in their details. Tian et al. (2009) showed N-S oriented high-velocity anomalies in the 80–300 km depth range. Lei (2012) showed an arc-shaped high-velocity anomaly extending from a shallow depth to 200 km. However, in the models of Huang and Zhao (2006), Li and van der Hilst (2010), and Obrebski et al. (2012), these high-velocity anomalies are confined to the 300–400, 150–350, and 100 km depth ranges, respectively. In this paper, H2′ and H2″ show complex morphologies, characterized as weak anomaly amplitudes of ~1% $\delta V_p/V_p$ or ~1.5% $\delta V_s/V_s$, and a region of relatively higher amplitude in the Yanshan Block. Compared with former models, our models also show some smaller-scale features. We detect the presence of a high-velocity anomaly (H3) under the Sulu Orogen (Figures 4a–f, 5a–f, 6k, and k′). Because of the much denser ray coverage for P-waves than S-waves in this region (Appendix Figures S6 and S7), the P-velocity model shows a relatively clearer velocity structure. H3's northern margin coincides with the Yantai-Qingdao-Wulian Fault and its western margin coincides with the Tan-Lu Fault, exhibiting a good tectonic correlation (Figures 4a–f and 5a–f).

3.4 Images in MTZ

H5 exists in the MTZ beneath the eastern NCC (Figures 4g–h, 5g–h, 6a–g, k, b′–g′, and k′), sharing the same features with previous models (e.g., Lebedev and Nolet, 2003; Huang and Zhao, 2006; Li et al., 2006, 2008; Tian et al., 2009; Feng et al., 2010; Li and van der Hilst, 2010; Lei, 2012; Obrebski et al., 2012; Zhao et al., 2012; Chen et al., 2015; Zhao D P et al., 2017). H5 is commonly interpreted as the stagnant slab

front of the subducted Pacific slab, but its specific morphology is still debated by different studies. Lei (2012) showed that the western edge of this high-velocity anomaly in the MTZ is at ~112°E, with a slab gap beneath the Datong volcano. Whereas the models of Huang and Zhao (2006), Tian et al. (2009), and Li and van der Hilst (2010) showed that this high-velocity anomaly lies flat in the MTZ and has its western edge at ~119°–120°E. Because of better ray coverage (Appendix Figures S6a–g and S7) and higher resolution (~168 km, Appendix Figures S9–S11 and discussed Section 4.1), our models' plan views (Figures 4g–h and 5g–h) demonstrate that the western edge of H5 is at ~118°E. From the vertical cross-sections (Figures 6a–g, k, b′–g′, and k′), we see that our models present some new morphological features of H5. H5 does not lie completely flat within the MTZ with some parts instead deflecting upward over 410-km discontinuities (Figures 6a–d, f–g, and f′; Wei et al., 2012). Additionally, some parts show slab bulking (Figures 6b, f, and f′) and some parts sink into the lower mantle though 660-km discontinuities with a western edge at ~116°E (Figures 6c–g, k, b′–g′, and k′, 7). In the area where H5 lies, the MTZ is obviously thickened (Chen and Ai, 2009; Xu et al., 2011; Zheng et al., 2017; Figures 6a–g, a′–g′, k, and k′).

4. Synthetic tests

In this paper, a series of synthetic tests have been performed to verify the reliability of major imaging features in our models. The synthetic test procedure is listed as follows. First, a synthetic velocity model was constructed in the model space. Second, synthetic traveltime delays for this synthetic velocity model were calculated using the same positions of stations and seismic events, and ray paths as those used in the inversion of observed data. Finally, these synthetic traveltime delays were inverted using the same inversion method and damping factor as the inversion of real seismic data. By comparing the synthetic model with its reconstructed model, we can evaluate where the resolution is good and where the resolution is poor. Two synthetic tests were conducted in this paper, the checkerboard resolution test and the restoring test.

4.1 Checkerboard resolution test

The checkerboard resolution test is used to assess resolution scale and regional ray coverage quality. We conducted various checkerboard resolution tests by applying alternating high- and low-velocity anomalies within individual blocks of different sizes, such as blocks four times the cell spacing (~134 km×138 km×91 km), five times the cell spacing (~168 km×173 km×114 km) and six times the cell spacing (~168 km×173 km×114 km). Anomaly amplitude of ±2% $\delta V_p/V_p$ and ±3% $\delta V_s/V_s$ were set to these blocks, and 10% Gaussian white noise was introduced to simulate observational errors in real seismic data. Appendix Figures S8–S11 show the checkerboard test results obtained using the same algorithm (LSQR method) and parameters (damping factors of 40.0 and 50.0 for P- and S-waves, respectively, and a convolutional quelling correlation length of two times the cell spacing) as in the real seismic data inversion.

Appendix Figure S8 shows the output model for an input block four times the size of the cell spacing. It shows reconstructed anomaly shapes can be recovered well, although some amplitudes are lost for P-waves in 30–300 km depth range (Figure S8a–c) and S-waves in 30–150 km depth range (Figure S8d–f). These results indicate that P- and S-waves have good spatial resolutions within 30–300 and 30–150 km depth ranges, respectively, and the resolution scale is ~134 km. For a block five times the size of cell spacing (resolution scale ~168 km), the regions showing good resolutions mainly dominate the 30–800 and 30–700 km depth ranges for P- and S-waves, respectively (Appendix Figures S9a–e, S10a–e for the P and Figures S9f–j and S10f–j for the S). Shown by the latitude slices of S-waves (Appendix Figures S10f–j), the output model exhibits better imaging results in the 30–250 and 400–700 km depth ranges than in the 250–400 km depth range, which may be because of the uneven ray density distribution for S-waves (Appendix Figure S6a′–h′). The output model for the block six times the size of cell spacing (resolution scale ~202 km) is illustrated in Appendix Figure S11. It shows that P- and S-waves have good spatial resolutions throughout the entire research area. In short, the checkerboard resolution tests show that P-waves dominate in resolution scales of~134 and ~168 km in the 30–300 and 300–800 km depth intervals, respectively, and that S-waves dominate resolution scales of ~134 and ~168 and 202 km in the 30–150, 150–700, and >700 km depth intervals, respectively.

4.2 Restoring test

Restoring tests have been applied to test the accuracy of morphological reconstruction for given input models and the extent of the smearing effect. By adjusting input velocity anomaly diameter and shape, several restoring tests were performed. The restoring test procedure is similar to that of the checkerboard resolution test. Based on imaging features of our models presented in Figures 4–6, several high- and low-velocity anomalies of varying diameters and dip angles were assigned to different depth ranges (outlined by gray dashed lines in Appendix Figure S12–S13). Velocity anomalies of ±2% $\delta V_p/V_p$ and ±3% $\delta V_s/V_s$ were introduced to each anomaly. As indicated by the reconstructed models, velocity anomaly amplitude and shape can be recovered well, with lateral resolution obviously better than vertical

resolution (Appendix Figures S12c–d, g–h, 3b, 13d, f, 13, and 13i–j), which is determined due to the nature of teleseismic tomography. Various tests show different effects of the base depth of velocity anomaly on the smearing effect extent. When the base depth of an anomaly is 200 km, the vertical smearing effect is very weak and can be neglected (H5 in Appendix Figure S13b and d; diameter and base depth are both 200 km for H5). However, the vertical smearing effect becomes obviously stronger for a model with its base depth at 280 km and smearing effect extent ~70 km (H1 in Appendix Figure S12c and g, diameter and base depth are 400 and 280 km for H1, respectively). In either a vertical or oblique form, the smearing effect is ~40 km for a velocity anomaly with a 410 km base depth (L1 in Appendix Figures S2c and g, L2 in Figure S13f and h, diameters and base depths for L1 and L2 are 400 and 410 km, respectively). However, the smearing effects are extremely pronounced when a high-velocity anomaly in the upper mantle is located above another high-velocity anomaly in the MTZ (Appendix Figure S12d and h). Therefore, high-velocity anomaly imaging features that penetrate from the upper mantle to the MTZ beneath the eastern NCC tend to be interpreted as smearing effect. We also tested the condition for a high-velocity anomaly in the MTZ located above another high-velocity anomaly in the lower mantle (H6 and H7 in Appendix Figure S13i and j; H6 is ~120°–124°E wide and 410–600 km depth; H7 is ~115.6°–120.6°E wide and 700–800 km depth). The reconstructed models show that these two anomalies can be clearly distinguished from each other, but show a certain extent of smearing effect because of abundant seismic rays coming from the east (Appendix Figure S7) and velocity anomalies on the eastern margin of research region (Figure S13i and j). Comparing reconstructed models' amplitudes obtained from restoring tests, recovered amplitudes of P-waves were reduced ~25% and recovered amplitudes of S-waves were reduced ~57%. This may account for differences in the images of P- and S-waves in the MTZ.

5. Discussions

In this paper, we obtained relative velocity perturbation values using zero-mean relative residuals; therefore, only the velocity contrasts between the anomalies are meaningful (Wawerzinek et al., 2013). A better understanding of lateral heterogeneity origins in seismic tomographic models would bring dynamic implications for inner Earth processes (Rocha et al., 2011). Temperature and composition, which stand for different dynamic processes, are considered the two of the most important factors involved in P- and S-velocity perturbations; however, it is not easy to distinguish these two factors' effects from only imaging results (Karato and Karki, 2001). Of these factors, temperature is considered the key factor causing upper mantle velocity perturbations based on petrophysical experiments and corresponding forward calculations (Goes et al., 2000; Cammarano et al., 2003; Hieronymus et al., 2007; Zhang et al., 2016). Whereas composition is a subordinate factor within a 400 km depth, and under a dry-mantle assumption, ±1% P-velocity perturbation approximately corresponds to a temperature variation exceeding 100–200 K (Cammarano et al., 2003). In the absence of intense depletion and Mg-rich harzburgites, the composition effect can be neglected, as it shows a velocity perturbation effect of <1% (Sobolev et al., 1995).

In addition to temperature, partial melting and fluids would also influence seismic parameters in tectonically active area (Anderson and Sammis, 1970; Artemieva et al., 2004). Partial melting could arise from heating and/or addition of fluids, and forward calculations show that each percentage point of partial melting in the upper mantle will cause at least a 3.6% P-velocity drop and 7.9% S-velocity drop (Hammond and Humphreys, 2000).

Inspections of our imaging results and the Lithosphere-Asthenosphere Boundary (LAB) depth derived from the receiver function both show that obvious low-velocity anomalies exist beneath regions in the eastern NCC where the lithosphere is notably thinned (Figure 6a–g, j, a′–g′, and j′). The pronounced and sharp lithosphere-asthenosphere transitions revealed by the receiver function suggest that these low-velocity anomalies are not only the result of temperature effects but are also accompanied by the effects of volatiles (gases and fluids) or partial melting (Rychert et al., 2005; Chen, 2010). Therefore, the velocity anomalies in this paper may result from a combination of temperature and fluids.

5.1 Pronounced lateral heterogeneities beneath the NCC

The lateral heterogeneities presented in our final P- and S-velocity models correspond with tectonic unit locations, the distribution of tectonic reactivation and magmatism, and regional dynamic events. The consistency of global features between our models and previous body-wave tomographic results (e.g., Huang and Zhao, 2006; Li et al., 2006, 2008; Sun et al., 2008a, 2008b; Tian et al., 2009; Zhao et al., 2009, 2012; Li and van der Hilst, 2010; Feng et al., 2010; Lei, 2012; Obrebski et al., 2012; Chen et al., 2015) suggests that our models are reliable, and meanwhile, we further revealed some new tectonic features. New models provide vital deep structural constraints for investigating the dynamic processes and spatial scales of lithospheric modification and thinning.

5.1.1 Limited destruction in the western NCC and TNCO

The Ordos Block is surrounded by the Inner Mongolia Suture Zone to the north, the Qilianshan Orogen to the west, the

Qinling Orogen to the south, and the TNCO to the east. Two elongate Cenozoic rift systems surround the Ordos Block: the arc-shaped Yinchuan-Hetao Rift to the northwest and the S-shaped Shaanxi-Shanxi Rift to the east and southeast. Imaging results show a high-velocity anomaly that extends downward to ~300 km beneath the Ordos Block (Figures 4a–f, 5a–f, 6a–e, i, a′–e′, and i′). Because of the vertical smearing effect, the actual depth of the Ordos Block is ~230 km (described in Section 4.2), which is similar to ~160–300 km lithospheric thickness obtained from the receiver function and surface wave tomography (denoted by solid black lines and contours in Figures 6 and 7, respectively; Bao et al., 2011; Chen et al., 2014; Jiang et al., 2013; Zheng et al., 2017). The Ordos Block is characterized by lower density (Li and Yang, 2011), lower surface heat flux (~40 mW m^{-2}; Wang J Y et al., 1996; Hu et al., 2000), and a lack of crustal deformation (Shen et al., 2000; Wang et al., 2003). This suggests the presence of Precambrian continental cores and their relative stability during multiple tectonic event stages. In contrast with the stable Ordos Block, intensive lithospheric extension and deformation are mainly concentrated in the Cenozoic rift systems throughout the western NCC and TNCO (Zhang Y Q et al., 1998; Zhang et al., 2003). Pronounced low-velocity anomalies occupy the upper mantle beneath these rift systems (Figures 4a–f and 5a–f) and are accompanied by regional thinning of the lithosphere and MTZ. The MTZ thickness was reduced to less than 245 km (Chen and Ai, 2009; green lines in Figures 6a–e, g–j, a′–e′, and g′–j′), whereas the lithospheric thickness is less than 100 km with spatial variation (Chen, 2010; contours in Figure 7a). As indicated by constraints from Cenozoic basalt geochemistry, the basalt magma sources became shallower with epoch going in the rift zones, reflecting that the lithosphere may have been continuously thinning during the Cenozoic (Xu et al., 2004, 2009; Xu, 2007).

The pre-existing structure in the lithosphere of the TNCO has been weakened and deformed to some extent, with lithospheric thickness varying from ~100 to 200 km, and the thinnest lithosphere found in the northern extension zone of the Shaanxi-Shanxi Rift (contours in Figure 7a). The Shaanxi-Shanxi Rift was reactivated at ~6 Ma, representing the latest stage of Cenozoic lithospheric thinning and modification (Wang N L et al., 1996, Zhang et al., 2003). Magmatism in the TNCO mainly occurred during the Late Cretaceous to Early Tertiary, which is much earlier than rift reactivation (Tang et al., 2006; Xu et al., 2008; Zhao et al., 2013). Our imaging results show that the low-velocity anomalies are not confined to the rift zone, but instead show a good spatial correspondence with the Honggeertu and Datong volcanoes (Figures 4a–f and 5a–f) and Cenozoic magmatic events (yellow circles in Figure 7b). Unlike the imaging features from the model of Lei (2012) that show noticeable low-velocity anomalies beneath the Datong volcano that extend downward to the lower mantle, our imaging features show L1 occupying a space from shallow depths to the top of the MTZ (Figure 6a–d, g–h, j, a′–d′, g′–h′, and j′; the same features are shown in Huang and Zhao, 2006; Li and van der Hilst, 2010; Zhao et al., 2012). However, in the S-velocity model, L1 extends much deeper, penetrating the MTZ at a depth of ~550 km (Figure 6a–d, g–h, j, a′–d′, g′–h′, and j′). It is not likely that this results from the vertical smearing effect judging by the restoring tests described in Section 4.2. We infer that this may reflect velocity changes resulting from a subducted slab and thermal and compositional changes in the MTZ (Schmandt and Humphreys, 2010). The exhibited NW-SE strike of L1 (Figures 4a–f and 5a–f) is consistent with GPS data (Wang et al., 2001), absolute plate motion direction (Gripp and Gordon, 2002), and fast axes of anisotropy (Huang et al., 2011; Chang et al., 2012). Horizontal mantle flow beneath the L1 region may account for this strike orientation, which was concluded using SKS splitting measurements (Huang et al., 2011; Zhao et al., 2011; Chang et al., 2012) and P-wave radial anisotropy tomography (Wang et al., 2014). L2 demonstrates obvious spatial differences from L1. It tapers off at ~200–300 km depth (Figure 6e–f, j, and j′), is accompanied by less Cenozoic magmatism (yellow circles in Figure 7b), keeps relatively thicker lithosphere of ~160–200 km (contours in Figure 7a), and is characterized as negative radial anisotropy (i.e., horizontal V_p< vertical V_p). By Inspecting the thinned MTZ beneath the TNCO (green dashed lines in Figure 6; Xu et al., 2011; Zheng et al., 2017), we can infer that L1 is related to the subducted Pacific slab (Huang and Zhao, 2006; Zhao, 2007; Zhao and Xue, 2010). However, the high-velocity anomaly between L1 and L2 (Figures 4a–f and 5a–f), adjacent to the transtensional zone of the Shaanxi-Shanxi Rift, cannot be definitively interpreted as part of the Ordos Block, or a lithospheric remnant of the TNCO (Jiang et al., 2013) limited by the lateral resolution scale.

5.1.2 Spatial heterogeneity of eastern NCC destruction

Like the Ordos Block, the eastern NCC is also surrounded by orogenic belts, with the Late Permian to Early Triassic CAOB to the north, the TNCO to the west, and the Qinling-Dabie-Sulu orogenic belt, which was formed by a Triassic collision, to the south and east. However, there is a difference in that lithosphere in the eastern NCC has been widely and significantly thinned. The lithospheric thickness of the eastern NCC ranges from ~60 to ~100 km (contours in Figure 7a; Chen et al., 2006, 2008; Chen, 2010; Li et al., 2013; Zheng et al., 2017), with the thinnest beneath the Tan-Lu Fault ~60–70km (contours in Figure 7a; Chen et al., 2006; Chen, 2010). Beneath the CAOB and Tan-Lu Fault are L4 and L3, respectively (Figures 4a–e and 5a–e). Geochemical studies show that the CAOB has experienced multiple stages of tectonic reactivation since the Late Car-

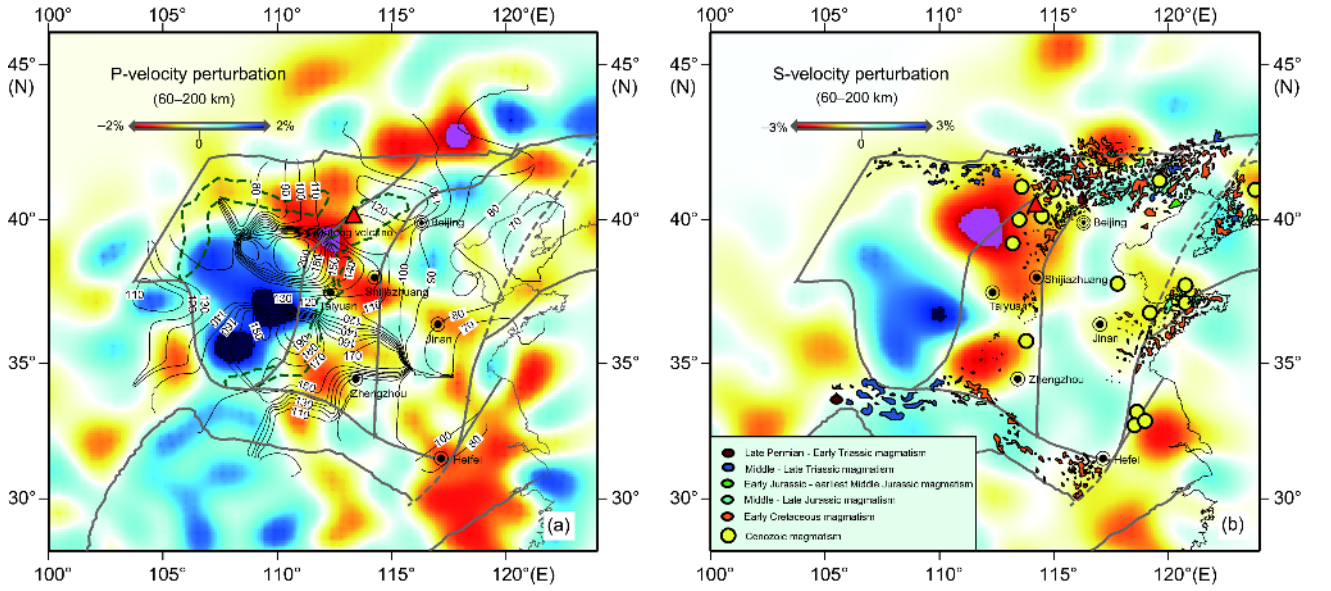

Figure 7 Map showing lithospheric thickness (a) and the temporal and spatial distribution of magmatism (b). The base maps of images (a) and (b) are the P- and S-wave averaged velocity perturbation within the 60–200 depth range, respectively. The depth values of Lithosphere-Asthenosphere Boundary interface are obtained from the receiver function (Zheng et al., 2017). The locations of magmatism in image (b) refer to the works of Wu et al. (2008), Xu et al. (2009) and Zhang et al. (2014).

boniferous (Li et al., 2009; Xu et al., 2009; Zhang et al., 2014; Figure 7b), whereas the Tan-Lu Fault is thought to have facilitated asthenospheric upwelling and lithospheric reactivation in the eastern NCC (Xu, 2001; Zheng et al., 2008; Chen, 2010). Geodynamic modeling results suggest that weak zones, such as orogenic belts and faults, can increase deep cratonic lithosphere longevity by buffering mantle-derived stresses acting on Archean cratons (Lenardic et al., 2000, 2003). Another frequently invoked mechanism that stabilizes cratons is high viscosity, which is characterized as a high brittle yield stress for cratonic lithosphere (Lenardic et al., 2003; Hieronymus et al., 2007). However, this mechanism cannot provide stability and lithospheric longevity for cratons that come into contact with subduction zones (Lenardic et al., 2003). The tectonic evolution differences between the western NCC and the eastern NCC may reflect differences in near-field and far-field influences of the subduction of the Pacific plate.

In the region surrounded by L1, L2, L3, and L4, H2′ and H2″ are visible beneath the eastern NCC (Figures 4a–e, 5a–c, 6a–c, e, g, k, a′ –c′, e′, g′, and k′). H2′, which is beneath the Yanshan Block, exhibits a higher anomaly amplitude than H2″. Surface wave imaging also detected high-velocity anomalies in this region with absolute S-wave speeds of ~4.45–4.6 km s^{-1}, which is a typical craton velocity value (Tang and Chen, 2008). Unlike the high heat flow values (~60–75 mW m^{-2}) presented in other parts of the eastern NCC, surface heat flow in the Yanshan Block region is ~30–50 mW m^{-2} (Hu et al., 2000, 2001; Wang, 2001), which corresponds to a thicker "hot" lithosphere (~100–120 km) (He et al., 2001) and is in accordance with the lithosphere thickness (~80–110 km, >120 km locally; Figure 6b) obtained from the receiver function (e.g., Chen, 2010; Zheng et al., 2017). Studies of igneous rocks found adakites with less 100 Ma old in the Yanshan region, which suggests that this area might have been in a weak extensional tectonic setting (Davis, 2003). These observations also suggest that a thick cratonic mantle root could have been preserved under the Yanshan Block, and that the region in which modification is not obvious. H2″ is mainly located in the eastern NCC portion enclosed by the cities of Shijiazhuang, Zhengzhou, Hefei and Jinan. Tian et al. (2009) and Lei (2012) also showed high-velocity anomalies in this area. Previous studies of mantle xenoliths from Cenozoic basalts revealed that the lithosphere in the Hebi area could be interpreted as shallow relics of an Archean mantle root (Zheng et al., 2001, 2007; Tang et al., 2013). Gravity inversion data showed negative density anomalies in the 60–160 km depth range in this region, which are characterized as having lower density (Li and Yang, 2011). It is predicted from the petrological data that cratonic areas have an average lithospheric mantle density of 1.5–2.5%, which is less dense than non-cratonic areas at the same temperature and pressure (Poudjom Djomani et al., 2001) and the cratons are characterized by a lower density of ~3.3 g cm^{-3} (Zhu R X et al., 2012a). We therefore infer that H2″, a high-velocity and low-density anomaly, is a refractory Archean lithosphere. Recent receiver function studies reveal that a complex layered structure exists beneath this region, namely the Paleoproterozoic slab of the western NCC, which penetrated the eastern Archean li-

thosphere remnant at a ~20°angle. Redox melting may have taken place along weak belts in the lithosphere like incisions and shear zones during craton destruction, resulting in short partial melting belts (Wang et al., 2013). A reasonable explanation for H2″ having a weak amplitude is that these partial melting belts are smaller than the seismic resolution scale, but still affect observed travel times.

5.2 Dynamic implications from the heterogeneity of eastern NCC destruction

The small-scale lateral heterogeneities revealed in the eastern NCC are the most intriguing imaging features in this paper. These features not only show excellent spatial correlation with orogens at the surface, they also exhibit good vertical consistency in the 60–250 km depth range (Figures 4a–e and 5a–e). Our analyses in Section 5.1.2 showed that these small-scale heterogeneities may have resulted from spatially non-uniform destruction of the eastern NCC. Therefore, a new scientific issue arises: what is the dynamic implication of the heterogeneities observed in the eastern NCC by seismic tomography?

The high-velocity anomalies detected in the MTZ (Figures 4a–h, 5g–h, 6a–g, k, b′–g′, and k′) are interpreted as the stagnant front of the subducted Pacific slab (e.g., Lebedev and Nolet, 2003; Huang and Zhao, 2006; Li et al., 2006, 2008; Tian et al., 2009; Li and van der Hilst, 2010; Xu and Zhao, 2009; Feng et al., 2010; Lei, 2012; Obrebski et al., 2012; Zhao et al., 2012; Chen et al., 2015). High-velocity anomalies within the MTZ that our models revealed show multi-scale lateral variations (Figure 6a–g, k, b′–g′, and k′). Because of differences in reconstruction ability between P- and S-waves as described in Section 4.2, high-velocity anomalies presented in the P- and S-velocity models share some common features, though some differences exist. For example, if high-velocity anomalies in the MTZ represent the stagnant subducted Pacific slab, then the slab front is located at ~118°E (Figures 4g–h and 5g–h). Another apparent common feature is that parts of the high-velocity anomalies between 116°E and 120°E penetrated 660-km discontinuities sunk into the lower mantle (Figures 6b–f and b′–f′). The heterogeneous morphologies of these high-velocity anomalies indicate that buckling and/or fragmentation of subducted oceanic slab may have occurred in the MTZ (Schmid et al., 2002; Ribe et al., 2007; Čížkov and Bina, 2013). Oceanic slab subduction into the water-rich MTZ (Kuritani et al., 2011) would trigger dehydration, meaning that the water could be from the subducted slab, the MTZ, or both. Morphological changes of the subducted slab, such as buckling, fragmentation, and local subsidence, would also enhance dehydration. Geodynamic modeling results show that dehydration associated with plate subduction is spatially heterogeneous. Dehydration could lead to partial melting at the top of the MTZ, triggering wet upwellings (melt from light hydrous or partial melting melt). Such vertical wet upwellings could be deflected by surrounding mantle flow, resulting in extensive mantle flow heterogeneities (Yang et al., 2017). The non-uniform distribution of low-velocity anomalies in the 200–400 km depth range of the upper mantle (Figures 4e–f, 5e–f, and 6) may be results of non-uniform distribution of lighter partial melting.

Areas, in the L1 region, with anomaly amplitudes of >2% $\delta V_p/V_p$ or >3% $\delta V_s/V_s$ are confined to ~60–250 km depth range beneath the TNCO and show a NW–SE strike. In addition, the largest scale for S-waves is ~400 km×100 km (Figures 4a–f, 5a–f, 6b, j, a'–c', g'–h', and j'). The V_p/V_s ratio model of Zhao et al. (2012) found a $\delta\ln V_s/\delta\ln V_p$ value of ~2.4 in this area. From calculations of $\delta\ln V_s/\delta\ln V_p$ based on petrological experiments, the expected value for thermal variations in the upper mantle ranges from 1.3 to 2.2 at low and high temperatures, respectively (Cammarano et al., 2003). We therefore infer that the $\delta\ln V_s/\delta\ln V_p$ value of the L1 region may reflect partial melting in the upper mantle, and an anomaly amplitude of >2% $\delta V_p/V_p$ or >3% $\delta V_s/V_s$ approximately corresponds to partial melting of 1–2% (Hammond and Humphreys, 2000). Alkali basalt (resulting from a small degree of partial melting from upwelling asthenoshphere) and tholeiitic basalt (resulting from a large degree of partial melting at shallower depths involving large amounts of eroded, enriched lithospheric mantle) geographical distributions in the Datong volcanic region exhibit good consistency with L1's strike, gradually transitioning from tholeiitic basalt in the southeast to alkali basalt in the northwest (Xu et al., 2005). Ascending partial melting could be subject to LAB fluctuation, inducing an edge-driven convection (As described in Section 5.1.1, many studies revealed a horizontal mantle flow under the Datong region. e.g., Huang et al., 2011; Zhao et al., 2011; Chang et al., 2012; Wang et al., 2014), and resulting in small-scale upwelling, which may be responsible for volcanism in this area (Xu et al., 2005; Wang and Niu, 2011). This small lateral scale of convection may suggest a shallow origin near the LAB for volcanism occurring at Datong (Wang and Niu, 2011). The vertical cross-sections of our models (Figure 6b, j, a′–c′, g′–h′, and j′) show the LAB interface morphologies acquired from the receiver function cross the L1 region with a larger anomaly amplitude (>2% $\delta V_p/V_p$ or >3% $\delta V_s/V_s$). This observational feature may indicate an accumulation of lighter partial melt at the LAB over time (Sakamaki et al., 2013). Accumulated melt could interact with the lithospheric mantle, resulting in its re-enrichment. Therefore, the extensive heterogeneities exhibited in the eastern NCC may have resulted from episodic melting and fluid-induced enrichment of the Archean mantle (Tang et al., 2013). Recent studies on water content and oxygen isotopic composition of alkali basalt suggest that partial melting and fluids are largely

contributed by the dehydration of Pacific oceanic slab and recycled oceanic crust along with entrained sediments (Liu et al., 2015). Dynamic processes beneath the TNCO may be a microcosm of the eastern NCC destruction.

Geodynamic modeling results show no clear spatial or temporal trend in magmatism development within the craton because of the complex mantle flow caused by partial melting (Yang et al., 2017). The distribution of exposed magmatism (Figure 7b) shows that Late Permian to Late Jurassic magmatism was mainly distributed in the orogenic belts around the NCC. However, Early Cretaceous magmatism corresponding to the peak of craton destruction extended from surrounding orogenic belts to the NCC interior, including both the TNCO and both sides of the Tan-Lu Fault (Xu et al., 2009; Zhang et al., 2014). The orogenic belts surrounding the NCC, the TNCO, and the Tan-Lu Fault are characterized by low-velocity anomalies (Figures 4a–4d and 5a–5d) that show a good spatial correspondence with the distribution of exposed magmatism from the Late Permian to the Cenozoic (Figure 7b). This suggests that a clear tectonic correlation for magmatism in the NCC exists. Because the work of Yang et al. (2017) did not consider the influence of lithospheric inner structure (e.g., orogenic belts and faults), the difference between the tectonic correlation of magmatism and dynamic modeling results indicates that internal structure of the lithosphere may play a key role in craton destruction (Xu et al., 2009; Chen, 2010). Gold deposits in the NCC are called "decratonic gold deposits" for the reason of the close relationship between their origins and craton destruction, and their distribution having a good spatial consistency with Early Cretaceous magmatism mainly along two NNE-trending bands of the TNCO and the Tan-Lu Fault. The orogenic belts and Tan-Lu Fault may provide favorable space for ore-forming fluids to circulate and precipitate (Zhu et al., 2015, 2017).

Based on above analyses, we can infer that wet upwellings-induced lithospheric re-enrichment, which was triggered by subducted Pacific slab, is the mechanism of the NCC destruction (Wang et al., 2015; Yang et al., 2017). Figure 8 is a sketch map showing the dynamic processes of the NCC destruction. During the Late Mesozoic, the subducted Pacific slab beneath the NCC caused non-uniform dehydration, which induced partial melting at the top of the MTZ, triggering wet upwellings. Ascending wet upwellings (light hydrous melt and partial melting melt) showed spatial heterogeneities and caused complex flows in the upper mantle in the 200–410 km depth range. When the lighter melt encountered the stable cratonic lithosphere root it would accumulate at the LAB, with some melt continuing to rise through relatively weak zones in lithosphere such as orogenic belts and faults. Therefore, the heterogeneities exhibited in the eastern NCC may result from the combined

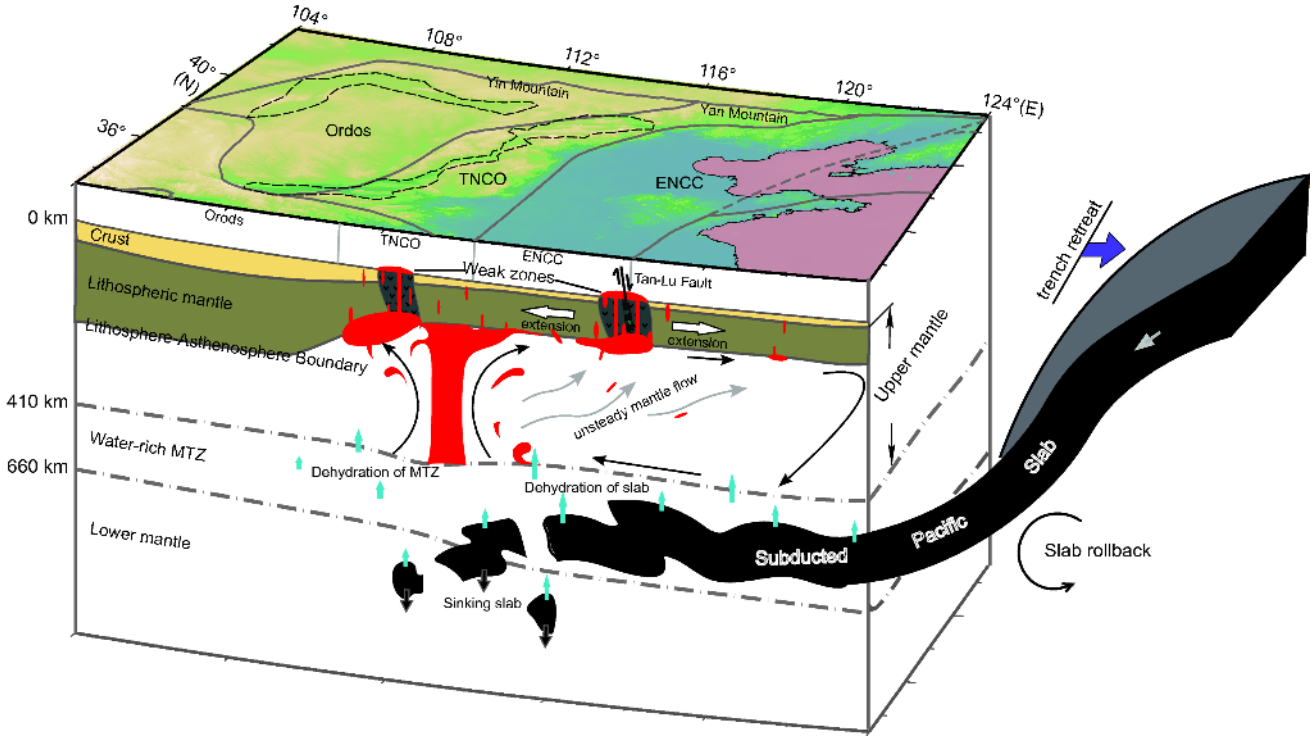

Figure 8 Cartoon map showing NCC destruction processes. This cartoon map was modified referring to the model from Zhu et al. (2015). It was drawn based on the tomographic results in this paper, wet upwellings triggered by dehydration from the water-rich MTZ (Kuritani et al., 2011) and subducted Pacific slab (Wang et al., 2015; Yang et al., 2017), the melt accumulation at the LAB (Sakamaki et al., 2013), the distributions of gold deposits (Zhu et al., 2015, 2017), and the distributions of magmatism since Mesozoic (Xu et al., 2009; Zhang et al., 2014).

effects of the spatially non-uniform distribution of wet upwellings in the upper mantle and pre-existing weak zones in cratonic lithosphere.

5.3 Upper mantle images of the Sulu ultrahigh pressure metamorphic belt

H3 is visible beneath the Sulu orogenic belt within 200 km depth in our models and appears to be controlled by the Yantai-Qingdao-Wulian and Tan-Lu faults (Figures 4a–d and 5a–d). An intense sinistral displacement of ~550 km along the Tan-Lu Fault between the Dabie and Sulu orogens is the result of the long-term evolution of a Mesozoic syn-collisional transform fault to a Cenozoic strike-slip fault (Zhu G et al., 2005, 2009). H3 exhibits a N-E-N orientation morphologically, and its western part has a larger amplitude and extends downward to ~300 km (Figures 4a–f). These imaging features may be related to counterclockwise rotation of the Yangtze Craton during the Triassic collision with the NCC (Gilder et al., 1999; Zhu G et al., 2009). Based on the location of high pressure-ultrahigh pressure (HP-UHP) metamorphic rocks and petrologic evidence, the Sulu orogen belongs to a part of the Yangtze Craton (Faure et al., 2003). From studies of Late Cretaceous basalts in Junan area, the occurrence of high-$Mg^{\#}$ mantle peridotitic xenoliths suggests that old refractory lithospheric mantle remnants may be still preserved beneath this region (Ying et al., 2006). H3 may thus represent a remnant of the Yangtze Craton which was subducted northwestward, and the Yantai-Qingdao-Wulian Fault may be the northern subduction margin of the Yangtze Craton.

6. Conclusions

We obtained new high-resolution 3-D P- and S-velocity models of the NCC using a multi-frequency joint inversion technique. Our models show obvious lateral heterogeneities and have a good spatial correspondence with tectonic units:

(1) Beneath the Ordos Block is a high-velocity anomaly that extends downward to a depth of ~300 km, representing the old Archean cratonic lithospheric root. In contrast, the Cenozoic Yinchuan-Hetao and Shaanxi-Shanxi rifts around the Ordos Block are characterized by low-velocity anomaly, which may have resulted from Cenozoic tectonic reactivation in these areas.

(2) The TNCO exhibits low-velocity anomaly, with significantly stronger anomaly amplitudes than in the eastern NCC. It also shows spatial differences between its northern and southern parts. The northern low-velocity anomaly corresponds to Quaternary volcanic groups (e.g., Datong volcano) with a NW-SE strike and extends downward to the MTZ. However, the southern low-velocity anomaly tapers off at ~200–300 km depth. Multidisciplinary evidence suggests that the low-velocity anomalies in the TNCO are closely related to the subducted Pacific slab. Additionally, we detected a small high-velocity patch between the northern and southern low-velocity anomalies adjacent to the transtensional zone of the Shaanxi-Shanxi Rift.

(3) Compared to the western NCC and TNCO, the eastern NCC exhibits small-scale heterogeneities in the upper mantle, which indicates spatially non-uniform destruction of the eastern NCC. A low velocity anomaly is detected beneath the Tan-Lu Fault, extending downward to ~200–300 km depth. However, the southern part and northern Yanshan Block region of the eastern NCC show high-velocity anomalies with weak anomaly amplitudes, which may represent the remnants of craton lithosphere. To the east, a high-velocity anomaly is revealed beneath the Sulu Orogen occupying the space within a ~300 km depth, and its northern and western margins coincide with the Yantai-Qingdao-Wulian and the Tan-Lu faults, respectively.

(4) A high-velocity anomaly showing morphological heterogeneities is visible in the MTZ, which represents the stagnant front of the subducted Pacific slab. Its western front is located at ~118°E, and parts of this high-velocity anomaly, mainly located around 116°–120°E, penetrate the 660-km discontinuities.

The combined analyses of our new imaging models with receiver function imaging (Chen, 2010; Zheng et al., 2017), shallow geologic observations (Xu et al., 2009; Zhang et al., 2014), studies of gold deposits (Zhu et al., 2015, 2017), and geodynamic numerical modeling experiments (Yang et al., 2017), allow us to infer that the lateral small-scale heterogeneities in the eastern NCC are a combined result of wet upwellings triggered by Pacific slab subduction and pre-existing weak zones (e.g., orogenic belts and the Tan-Lu Fault) in the cratonic lithosphere. In our models, the Sulu UHP metamorphic belt is at the edge of the study area, and the resolution test shows the reliability of the velocity structure in this region. However, a finer regional velocity model is necessary to better understand the development of the Tan-Lu Fault and the collision of the NCC and the Yangtze Craton, and depends on further work.

Acknowledgements *We thank Prof. Xiufen Zheng from Institute of Geophysics, China Earthquake Administration, and colleagues from the Seismological Laboratory of the Institute of Geology and Geophysics, Chinese Academy of Sciences, and colleagues from Peking University for their hard work of data collection. We thank Dr. Huaiyu Yuan, Xiaofeng Liang and Fengxue Zhang for their helpful suggestions. We are grateful to Yaoyang Zhang for providing the latest data of the LAB interface depth. We appreciate Editorial Board and three anonymous reviewers for their constructive comments and suggestions. Waveform data are provided by Seismological Laboratory, IGGCAS and Data Management Centre of China National Seismic Network at Institute of Geophysics, Chinese Earthquake Administration. This research was supported by National Key Research and*

Development Program of China (Grant No. 2017YFC0601206).

References

Anderson D L, Sammis C. 1970. Partial melting in the upper mantle. Phys Earth Planet Inter, 3: 41–50

Allen R M, Nolet G, Morgan W J, Vogfjörd K, Bergsson B H, Erlendsson P, Foulger G R, Jakobsdóttir S, Julian B R, Pritchard M, Ragnarsson S, Stefánsson R. 2002. Imaging the mantle beneath Iceland using integrated seismological techniques. J Geophys Res, 107: 3-1–3-16

Artemieva I M, Mooney W D. 2001. Thermal thickness and evolution of Precambrian lithosphere: A global study. J Geophys Res, 106: 16387–16414

Artemieva I M, Billien M, Lévêque J J, Mooney W D. 2004. Shear wave velocity, seismic attenuation, and thermal structure of the continental upper mantle. Geophys J Int, 157: 607–628

Bao X, Xu M, Wang L, Mi N, Yu D, Li H. 2011. Lithospheric structure of the Ordos Block and its boundary areas inferred from Rayleigh wave dispersion. Tectonophysics, 499: 132–141

Cammarano F, Goes S, Vacher P, Giardini D. 2003. Inferring upper-mantle temperatures from seismic velocities. Phys Earth Planet Inter, 138: 197–222

Chang L, Wang C Y, Ding Z. 2012. Upper mantle anisotropy beneath North China from shear wave splitting measurements. Tectonophysics, 522-523: 235–242

Chen L. 2010. Concordant structural variations from the surface to the base of the upper mantle in the North China Craton and its tectonic implications. Lithos, 120: 96–115

Chen L, Ai Y S. 2009. Discontinuity structure of the mantle transition zone beneath the North China Craton from receiver function migration. J Geophys Res, 114: B06307

Chen L, Jiang M, Yang J, Wei Z, Liu C, Ling Y. 2014. Presence of an intralithospheric discontinuity in the central and western North China Craton: Implications for destruction of the craton. Geology, 42: 223–226

Chen L, Tao W, Zhao L, Zheng T Y. 2008. Distinct lateral variation of lithospheric thickness in the Northeastern North China Craton. Earth Planet Sci Lett, 267: 56–68

Chen L, Zheng T, Xu W. 2006. A thinned lithospheric image of the Tanlu Fault Zone, eastern China: Constructed from wave equation based receiver function migration. J Geophys Res, 111: B09312

Chen M, Niu F, Liu Q, Tromp J, Zheng X. 2015. Multiparameter adjoint tomography of the crust and upper mantle beneath East Asia: 1. Model construction and comparisons. J Geophys Res-Solid Earth, 120: 1762–1786

Chevrot S, Villaseñor A, Sylvander M, Benahmed S, Beucler E, Cougoulat G, Delmas P, de Saint Blanquat M, Diaz J, Gallart J, Grimaud F, Lagabrielle Y, Manatschal G, Mocquet A, Pauchet H, Paul A, Péquegnat C, Quillard O, Roussel S, Ruiz M, Wolyniec D. 2014. High-resolution imaging of the Pyrenees and Massif Central from the data of the PYROPE and IBERARRAY portable array deployments. J Geophys Res-Solid Earth, 119: 6399–6420

Čížková H, Bina C R. 2013. Effects of mantle and subduction-interface rheologies on slab stagnation and trench rollback. Earth Planet Sci Lett, 379: 95–103

Dahlen F A, Hung S H, Nolet G. 2000. Fréchet kernels for finite-frequency traveltimes-I. Theory. Geophys J Int, 141: 157–174

Davis G A. 2003. The Yanshan belt of North China: Tectonics, adakitic magmatism, and crustal evolution. Earth Sci Front, 10: 373–384

Davies J H. 2013. Global map of solid Earth surface heat flow. Geochem Geophys Geosyst, 14: 4608–4622

Davis G A, Zheng Y, Wang C, Darby B J, Zhang C, Gehrels G. 2001. Mesozoic tectonic evolution of the Yanshan fold and thrust belt, with emphasis on Hebei and Liaoning provinces, northern China. In: Hendrix M S, Davis G A, eds. Paleozoic and Mesozoic Tectonic Evolution of Central and Eastern Asia. Mem Geol Soc Am, 194: 171–197

Deng J F, Mo X X, Zhao H L, Luo Z H, Du Y S. 1994. Lithosphere root/deep rooting and activation of the east China continent (in Chinese). Geoscience, 8: 349–356

Ekström G, Dziewonski A M. 1998. The unique anisotropy of the Pacific upper mantle. Nature, 394: 168–172

Faure M, Lin W, Monié P, Le Breton N, Poussineau S, Panis D, Deloule E. 2003. Exhumation tectonics of the ultrahigh-pressure metamorphic rocks in the Qinling orogen in east China: New petrological-structural-radiometric insights from the Shandong Peninsula. Tectonics, 22: 1018

Feng M, van der Lee S, An M J, Zhao Y. 2010. Lithospheric thickness, thinning, subduction, and interaction with the asthenosphere beneath China from the joint inversion of seismic S-wave train fits and Rayleigh-wave dispersion curves. Lithos, 120: 116–130

Gao S, Rudnick R L, Yuan H L, Liu X M, Liu Y S, Xu W L, Ling W L, Ayers J, Wang X C, Wang Q H. 2004. Recycling lower continental crust in the North China craton. Nature, 432: 892–897

Gilder S A, Leloup P H, Courtillot V, Chen Y, Coe R S, Zhao X, Xiao W, Halim N, Cogné J P, Zhu R. 1999. Tectonic evolution of the Tancheng-Lujiang (Tan-Lu) fault via Middle Triassic to Early Cenozoic paleomagnetic data. J Geophys Res, 104: 15365–15390

Goes S, Govers R, Vacher P. 2000. Shallow mantle temperatures under Europe from P and S wave tomography. J Geophys Res, 105: 11153–11169

Griffin W L, Andi Z, O'Reilly S Y, Ryan C G. 1998. Phanerozoic evolution of the lithosphere beneath the Sino-Korean craton. Mantle Dynamics and Plate Interactions in East Asia. 107–126

Gripp A E, Gordon R G. 2002. Young tracks of hotspots and current plate velocities. Geophys J Int, 150: 321–361

Guillot S, Hattori K, Agard P, Schwartz S, Vidal O. 2009. Exhumation processes in oceanic and continental subduction contexts: A review. In: Lallemand S, Funiciello F, eds. Subduction zone geodynamics. Berlin: Springer. 175–205

Hammond W C, Humphreys E D. 2000. Upper mantle seismic wave velocity: Effects of realistic partial melt geometries. J Geophys Res, 105: 10975–10986

He L J, Hu S B, Wang J Y. 2001. The thermal structure features of lithosphere beneath eastern China (in Chinese). Prog Nat Sci, 11: 966–969

Hieronymus C F, Shomali Z H, Pedersen L B. 2007. A dynamical model for generating sharp seismic velocity contrasts underneath continents: Application to the Sorgenfrei-Tornquist Zone. Earth Planet Sci Lett, 262: 77–91

Hu S B, He L J, Wang J Y. 2000. Heat flow in the continental area of China: A new data set. Earth Planet Sci Lett, 179: 407–419

Hu S B, He L J, Wang J Y. 2001. Compilation of heat flow data in the China continental area. Chin J Geophys, 44: 604–618

Huang J L, Zhao D P. 2004. Crustal heterogeneity and seismotectonics of the region around Beijing, China. Tectonophysics, 385: 159–180

Huang J L, Zhao D P. 2006. High-resolution mantle tomography of China and surrounding regions. J Geophys Res, 111: B09305

Huang Z, Wang L, Zhao D, Mi N, Xu M. 2011. Seismic anisotropy and mantle dynamics beneath China. Earth Planet Sci Lett, 306: 105–117

Hung S H, Dahlen F A, Nolet G. 2000. Fréchet kernels for finite-frequency traveltimes-II. Examples. Geophys J Int, 141: 175–203

Hung S H, Shen Y, Chiao L Y. 2004. Imaging seismic velocity structure beneath the Iceland hot spot: A finite frequency approach. J Geophys Res, 109: B08305

Jiang M M, Ai Y S, Chen L, Yang Y J. 2013. Local modification of the lithosphere beneath the central and western North China Craton: 3-D constraints from Rayleigh wave tomography. Gondwana Res, 24: 849–864

Karato S I, Karki B B. 2001. Origin of lateral variation of seismic wave velocities and density in the deep mantle. J Geophys Res, 106: 21771–21783

Kennett B L N, Engdahl E R. 1991. Traveltimes for global earthquake location and phase identification. Geophys J Int, 105: 429–465

Koulakov I, Kaban M K, Tesauro M, Cloetingh S. 2009. *P*- and *S*-velocity anomalies in the upper mantle beneath Europe from tomographic inversion of ISC data. Geophys J Int, 179: 345–366

Kuritani T, Ohtani E, Kimura J I. 2011. Intensive hydration of the mantle transition zone beneath China caused by ancient slab stagnation. Nat Geosci, 4: 713–716
Lebedev S, Nolet G. 2003. Upper mantle beneath Southeast Asia from *S* velocity tomography. J Geophys Res, 108: 2048
Lei J. 2012. Upper-mantle tomography and dynamics beneath the North China Craton. J Geophys Res, 117: B06313
Lei J, Xie F, Lan C, Xing C, Ma S. 2008. Seismic images under the Beijing region inferred from P and PmP data. Phys Earth Planet Inter, 168: 134–146
Lei J, Xie F, Fan Q, Santosh M. 2013. Seismic imaging of the deep structure under the Chinese volcanoes: An overview. Phys Earth Planet Inter, 224: 104–123
Lenardic A, Moresi L, Mühlhaus H. 2000. The role of mobile belts for the longevity of deep cratonic lithosphere: The Crumple Zone Model. Geophys Res Lett, 27: 1235–1238
Lenardic A, Moresi L N, Mühlhaus H. 2003. Longevity and stability of cratonic lithosphere: Insights from numerical simulations of coupled mantle convection and continental tectonics. J Geophys Res, 108: 2303
Li C, van der Hilst R D. 2010. Structure of the upper mantle and transition zone beneath Southeast Asia from traveltime tomography. J Geophys Res, 115: B07308
Li C, van der Hilst R D, Engdahl E R, Burdick S. 2008. A new global model for P wave speed variations in Earth's mantle. Geochem Geophys Geosyst, 9: Q05018
Li C, van der Hilst R D, Toksöz M N. 2006. Constraining P-wave velocity variations in the upper mantle beneath Southeast Asia. Phys Earth Planet Inter, 154: 180–195
Li S G, Xiao Y L, Liou D L, Chen Y Z, Ge N J, Zhang Z Q, Sun S S, Cong B L, Zhang R Y, Hart S R, Wang S S. 1993. Collision of the North China and Yangtse Blocks and formation of coesite-bearing eclogites: Timing and processes. Chem Geol, 109: 89–111
Li H Y, Xu Y G, Huang X L, He B, Luo Z Y, Yan B. 2009. Activation of northern margin of the North China Craton in Late Paleozoic: Evidence from U-Pb dating and Hf isotopes of detrital zircons from the Upper Carboniferous Taiyuan Formation in the Ningwu-Jingle basin. Chin Sci Bull, 54: 677–686
Li Y, Yang Y. 2011. Gravity data inversion for the lithospheric density structure beneath North China Craton from EGM 2008 model. Phys Earth Planet Inter, 189: 9–26
Li Y, Wu Q, Pan J, Zhang F, Yu D. 2013. An upper-mantle S-wave velocity model for East Asia from Rayleigh wave tomography. Earth Planet Sci Lett, 377-378: 367–377
Liang X, Shen Y, Chen Y J, Ren Y. 2011. Crustal and mantle velocity models of southern Tibet from finite frequency tomography. J Geophys Res, 116: B02408
Liu D Y, Nutman A P, Compston W, Wu J S, Shen Q H. 1992. Remnants of ≥3800 Ma crust in the Chinese part of the Sino-Korean craton. Geology, 20: 339–342
Liu J, Xia Q K, Deloule E, Ingrin J, Chen H, Feng M. 2015. Water content and oxygen isotopic composition of alkali basalts from the Taihang Mountains, China: Recycled oceanic components in the mantle source. J Petrol, 56: 681–702
Meyerholtz K A, Pavlis G L, Szpakowski S A. 1989. Convolutional quelling in seismic tomography. Geophysics, 54: 570–580
Nolet G. 1985. Solving or resolving inadequate and noisy tomographic systems. J Comput Phys, 61: 463–482
Obrebski M, Allen R M, Zhang F X, Pan J T, Wu Q J, Hung S H. 2012. Shear wave tomography of China using joint inversion of body and surface wave constraints. J Geophys Res, 117
Paige C C, Saunders M A. 1982. LSQR: An algorithm for sparse linear equations and sparse least squares. ACM Trans Math Softw, 8: 43–71
Pan G T, Mo X X, Hou Z Q, Zhu D C, Wang L Q, Li G M, Zhao Z D, Geng Q R, Liao Z L. 2006. Spatial-temporal framework of the Gangdese Orogenic Belt and its evolution. Acta Petrol Sin, 22: 521–533
Polet J, Anderson D L. 1995. Depth extent of cratons as inferred from tomographic studies. Geology, 23: 205–208
Poudjom Djomani Y H, O'Reilly S Y, Griffin W L, Morgan P. 2001. The density structure of subcontinental lithosphere through time. Earth Planet Sci Lett, 184: 605–621
Ren Y, Shen Y. 2008. Finite frequency tomography in southeastern Tibet: Evidence for the causal relationship between mantle lithosphere delamination and the north-south trending rifts. J Geophys Res, 113: B10316
Ribe N M, Stutzmann E, Ren Y, van der Hilst R. 2007. Buckling instabilities of subducted lithosphere beneath the transition zone. Earth Planet Sci Lett, 254: 173–179
Rocha M P, Schimmel M, Assumpção M. 2011. Upper-mantle seismic structure beneath SE and Central Brazil from P- and S-wave regional traveltime tomography. Geophys J Int, 184: 268–286
Rychert C A, Fischer K M, Rondenay S. 2005. A sharp lithosphere-asthenosphere boundary imaged beneath eastern North America. Nature, 436: 542–545
Sakamaki T, Suzuki A, Ohtani E, Terasaki H, Urakawa S, Katayama Y, Funakoshi K I, Wang Y, Hernlund J W, Ballmer M D. 2013. Ponded melt at the boundary between the lithosphere and asthenosphere. Nat Geosci, 6: 1041–1044
Schmandt B, Humphreys E. 2010. Complex subduction and small-scale convection revealed by body-wave tomography of the western United States upper mantle. Earth Planet Sci Lett, 297: 435–445
Schmid C, Goes S, van der Lee S, Giardini D. 2002. Fate of the Cenozoic Farallon slab from a comparison of kinematic thermal modeling with tomographic images. Earth Planet Sci Lett, 204: 17–32
Shen Z K, Zhao C, Yin A, Li Y, Jackson D D, Fang P, Dong D. 2000. Contemporary crustal deformation in east Asia constrained by Global Positioning System measurements. J Geophys Res, 105: 5721–5734
Sobolev S V, Zeyen H, Stoll G, Werling F, Altherr R, Fuchs K. 1995. Upper mantle temperatures from teleseismic tomography of French Massif Central including effects of composition, mineral reactions, anharmonicity, anelasticity and partial melt. Earth Planet Sci Lett, 139: 147–163
Sun Y S, Toksöz M N. 2006. Crustal structure of China and surrounding regions from P wave traveltime tomography. J Geophys Res, 111: B03310
Sun Y S, Toksöz M N, Pei S P, Zhao D, Morgan F D, Rosca A. 2008a. S wave tomography of the crust and uppermost mantle in China. J Geophys Res, 113: B11307
Sun Y S, Toksoz M N, Pei S P, Morgan F D. 2008b. The layered shear-wave velocity structure of the crust and uppermost mantle in China. Bull Seismol Soc Am, 98: 746–755
Tang Q, Chen L. 2008. Structure of the crust and uppermost mantle of the Yanshan Belt and adjacent regions at the northeastern boundary of the North China Craton from Rayleigh Wave Dispersion Analysis. Tectonophysics, 455: 43–52
Tang Y J, Zhang H F, Ying J F. 2006. Asthenosphere-lithospheric mantle interaction in an extensional regime: Implication from the geochemistry of Cenozoic basalts from Taihang Mountains, North China Craton. Chem Geol, 233: 309–327
Tang Y J, Zhang H F, Ying J F, Su B X, Chu Z Y, Xiao Y, Zhao X M. 2013. Highly heterogeneous lithospheric mantle beneath the Central Zone of the North China Craton evolved from Archean mantle through diverse melt refertilization. Gondwana Res, 23: 130–140
Tian Y, Zhao D. 2011. Destruction mechanism of the North China Craton: Insight from P and S wave mantle tomography. J Asian Earth Sci, 42: 1132–1145
Tian Y, Zhao D P, Sun R M, Teng J W. 2009. Seismic imaging of the crust and upper mantle beneath the North China Craton. Phys Earth Planet Inter, 172: 169–182
Van Decar J C, Crosson R S. 1990. Determination of teleseismic relative phase arrival times using multi-channel cross-correlation and least squares. Bull Seismol Soc of Amer, 80: 150–169
Wang J, Wu H, Zhao D P. 2014. P wave radial anisotropy tomography of the upper mantle beneath the North China Craton. Geochem Geophys Geosyst, 15: 2195–2210

Wang J Y, Huang S P, Chen M X. 1996. Terrestrial heat flux map (in Chinese). In: Yuan X C, ed. Geophysical Atlas in China. Beijing: Geophysical Publishing House. 102
Wang M, Shen Z K, Niu Z J, Zhang Z S, Sun H R, Gan W J, Wang Q, Ren Q. 2003. Contemporary crustal deformation of the Chinese continent and tectonic blockmodel. Sci China Ser D-Earth Sci, 46: 25–32
Wang N L, Yang J C, Xia Z K, Mo D W, Li Y L, Pan M. 1996. Cenozoic Sedimentary and Tectonic Features of Shanxi Garben (in Chinese). Beijing: Science Press
Wang P, Xu M, Wang L, Mi N, Yu D, Li H, Li C, Bao X, Huang T, Huang H. 2013. Seismic evidence for the stratified lithosphere in the south of the North China Craton. J Geophys Res-Solid Earth, 118: 570–582
Wang Q, Zhang P Z, Freymueller J T, Bilham R, Larson K M, Lai X, You X, Niu Z, Wu J, Li Y, Liu J, Yang Z, Chen Q. 2001. Present-day crustal deformation in China constrained by global positioning system measurements. Science, 294: 574–577
Wang X C, Wilde S A, Li Q L, Yang Y N. 2015. Continental flood basalts derived from the hydrous mantle transition zone. Nat Commun, 6: 7700
Wang X L, Niu F L. 2011. Imaging the mantle transition zone beneath eastern and central China with CEArray receiver functions. Earthq Sci, 24: 65–75
Wang Y. 2001. Heat flow pattern and lateral variations of lithosphere strength in China mainland: Constraints on active deformation. Phys Earth Planet Inter, 126: 121–146
Wawerzinek B, Ritter J R R, Roy C. 2013. New constraints on the 3D shear wave velocity structure of the upper mantle underneath Southern Scandinavia revealed from non-linear tomography. Tectonophysics, 602: 38–54
Wei W, Xu J, Zhao D, Shi Y. 2012. East Asia mantle tomography: New insight into plate subduction and intraplate volcanism. J Asian Earth Sci, 60: 88–103
Wu F Y, Xu Y G, Gao S, Zheng J P. 2008. Lithoshperic thinning and destruction of the North China Craton (in Chinese with English abstract). Acta Petrol Sin 24: 1145–1174
Wu F Y, Xu Y G, Zhu R X, Zhang G W. 2014. Thinning and destruction of the cratonic lithosphere: A global perspective. Sci China Earth Sci, 57: 2878–2890
Xiao W J, Windley B F, Hao J, Zhai M G. 2003. Accretion leading to collision and the Permian Solonker suture, Inner Mongolia, China: Termination of the central Asian orogenic belt. Tectonics, 22: 1069
Xiao W J, Windley B F, Yong Y, Yan Z, Yuan C, Liu C, Li J. 2009. Early Paleozoic to Devonian multiple-accretionary model for the Qilian Shan, NW China. J Asian Earth Sci, 35: 323–333
Xu P, Liu F, Ye K, Wang Q, Cong B, Chen H. 2002. Flake tectonics in the Sulu orogen in eastern China as revealed by seismic tomography. Geophys Res Lett, 29: 23-1–23-4
Xu P F, Zhao D P. 2009. Upper-mantle velocity structure beneath the North China Craton: Implications for lithospheric thinning. Geophys J Int, 177: 1279–1283
Xu W W, Zheng T Y, Zhao L. 2011. Mantle dynamics of the reactivating North China Craton: Constraints from the topographies of the 410-km and 660-km discontinuities. Sci China Earth Sci, 54: 881–887
Xu Y G. 2001. Thermo-tectonic destruction of the archaean lithospheric keel beneath the sino-korean craton in china: Evidence, timing and mechanism. Phys Chem Earth Part A-Solid Earth Geodesy, 26: 747–757
Xu Y G. 2007. Diachronous lithospheric thinning of the North China Craton and formation of the Daxin'anling-Taihangshan gravity lineament. Lithos, 96: 281–298
Xu Y G, Blusztajn J, Ma J L, Suzuki K, Liu J F, Hart S R. 2008. Late Archean to Early Proterozoic lithospheric mantle beneath the western North China craton: Sr-Nd-Os isotopes of peridotite xenoliths from Yangyuan and Fansi. Lithos, 102: 25–42
Xu Y G, Chung S L, Ma J, Shi L. 2004. Contrasting Cenozoic lithospheric evolution and architecture in the western and eastern Sino-Korean Craton: Constraints from geochemistry of basalts and mantle xenoliths. J Geol, 112: 593–605
Xu Y G, Ma J L, Frey F A, Feigenson M D, Liu J F. 2005. Role of lithosphere-asthenosphere interaction in the genesis of Quaternary alkali and tholeiitic basalts from Datong, western North China Craton. Chem Geol, 224: 247–271
Xu Y G, Li H Y, Pang C J, He B. 2009. On the timing and duration of the destruction of the North China Craton. Chin Sci Bull, 54: 3379
Yang J, Zhao L, Kaus B J P, Lu G, Wang K, Zhu R. 2017. Slab-triggered wet upwellings produce large volumes of melt: Insights into the destruction of the North China Craton. Tectonophysics
Yin A, Nie S Y. 1996. A Phanerozoic palinspastic reconstruction of China and its neighboring regions. In: Yin A, Harrison M, eds. The Tectonic Evolution of Asia. Cambridge: Cambridge University Press. 442–484
Ying J, Zhang H, Kita N, Morishita Y, Shimoda G. 2006. Nature and evolution of Late Cretaceous lithospheric mantle beneath the eastern North China Craton: Constraints from petrology and geochemistry of peridotitic xenoliths from Jünan, Shandong Province, China. Earth Planet Sci Lett, 244: 622–638
Zhang H F. 2009. Peridotite-melt interaction: A key point for the destruction of cratonic lithospheric mantle. Chin Sci Bull, 54: 3417–3437
Zhang K J. 1997. North and South China collision along the eastern and southern North China margins. Tectonophysics, 270: 145–156
Zhang M, Zhou X H, Zhang J B. 1998. Nature of the lithospheric mantle beneath NE China: Evidence from potassic volcanic rocks and mantle xenoliths. In: Griffin W L, Zhang A D, O'Reilly S Y, eds. Mantle Dynamics and Plate Interactions in East Asia. 197–219
Zhang S H, Zhao Y, Davis G A, Ye H, Wu F. 2014. Temporal and spatial variations of Mesozoic magmatism and deformation in the North China Craton: Implications for lithospheric thinning and decratonization. Earth-Sci Rev, 131: 49–87
Zhang Y, Wang Y, Zhao L, Jin Z. 2016. On velocity anomalies beneath southeastern China: An investigation combining mineral physics studies and seismic tomography observations. Gondwana Res, 31: 200–217
Zhang Y Q, Mercier J L, Vergély P. 1998. Extension in the graben systems around the Ordos (China), and its contribution to the extrusion tectonics of south China with respect to Gobi-Mongolia. Tectonophysics, 285: 41–75
Zhang Y Q, Ma Y S, Yang N, Shi W, Dong S. 2003. Cenozoic extensional stress evolution in North China. J Geodyn, 36: 591–613
Zhao D, Hasegawa A, Kanamori H. 1994. Deep structure of Japan subduction zone as derived from local, regional, and teleseismic events. J Geophys Res, 99: 22313–22329
Zhao D. 2007. Seismic images under 60 hotspots: Search for mantle plumes. Gondwana Res, 12: 335–355
Zhao D P, Isozaki Y, Maruyama S. 2017. Seismic imaging of the Asian orogens and subduction zones. J Asian Earth Sci, 145: 349–367
Zhao D P, Lei J S, Tang R. 2004. Origin of the Changbai intraplate volcanism in Northeast China: Evidence from seismic tomography. Chin Sci Bull, 49: 1401–1408
Zhao G, Wilde S A, Cawood P A, Sun M. 2001. Archean blocks and their boundaries in the North China Craton: Lithological, geochemical, structural and P-T path constraints and tectonic evolution. Precambrian Res, 107: 45–73
Zhao G C, Sun M, Wilde S A. 2003. Major tectonic units of the North China Craton and their Paleoproterozoic assembly. Sci China Ser D-Earth Sci, 46: 23–38
Zhao L, Allen R M, Zheng T, Hung S H. 2009. Reactivation of an Archean craton: Constraints from P- and S-wave tomography in North China. Geophys Res Lett, 36: L17306
Zhao L, Allen R M, Zheng T, Zhu R. 2012. High-resolution body wave tomography models of the upper mantle beneath eastern China and the adjacent areas. Geochem Geophys Geosyst, 13: Q06007
Zhao L, Paul A, Malusà M G, Xu X, Zheng T, Solarino S, Guillot S, Schwartz S, Dumont T, Salimbeni S, Aubert C, Pondrelli S, Wang Q, Zhu R. 2016. Continuity of the Alpine slab unraveled by high-resolution P wave tomography. J Geophys Res-Solid Earth, 121: 8720–8737
Zhao L, Xu X, Malusà M G. 2017. Seismic probing of continental subduction zones. J Asian Earth Sci, 145: 37–45

Zhao L, Xue M. 2010. Mantle flow pattern and geodynamic cause of the North China Craton reactivation: Evidence from seismic anisotropy. Geochem Geophys Geosyst, 11: Q07010
Zhao L, Zheng T, Lu G, Ai Y. 2011. No direct correlation of mantle flow beneath the North China Craton to the India-Eurasia collision: Constraints from new SKS wave splitting measurements. Geophys J Int, 187: 1027–1037
Zhao X M, Zhang H F, Su F, Hu Z C, Lo C H, Wang Y, Yang S H, Guo J H. 2013. Phlogopite $^{40}Ar/^{39}Ar$ geochronology of mantle xenoliths from the North China Craton: Constraints on the eruption ages of Cenozoic basalts. Gondwana Res, 23: 208–219
Zhao Y, Chen B, Zhang S H, Liu J M, Hu J M, Liu J, Pei J L. 2010. Pre-Yanshanian geological events in the northern margin of the North China Craton and its adjacent areas (in Chinese). Geol China, 37: 900–915
Zheng J, O'Reilly S Y, Griffin W L, Lu F, Zhang M, Pearson N J. 2001. Relict refractory mantle beneath the eastern North China block: Significance for lithosphere evolution. Lithos, 57: 43–66
Zheng J P, Griffin W L, O'Reilly S Y, Yu C M, Zhang H F, Pearson N, Zhang M. 2007. Mechanism and timing of lithospheric modification and replacement beneath the eastern North China Craton: Peridotitic xenoliths from the 100 Ma Fuxin basalts and a regional synthesis. Geochim Cosmochim Acta, 71: 5203–5225
Zheng T Y, Duan Y H, Xu W W, Ai Y S, Chen L, Zhao L, Zhang Y Y, Xu X B. 2017. Seismic velocity models of the crust-upper mantle beneath North China, v2.0. http://www.craton.cn/data
Zheng T Y, Zhao L, Xu W W, Zhu R X. 2008. Insight into modification of North China Craton from seismological study in the Shandong Province. Geophys Res Lett, 35: L22305
Zheng X F, Yao Z X, Liang J H, Zheng J. 2010. The role played and opportunities provided by IGP DMC of China National seismic network in Wenchuan Earthquake disaster relief and researches. Bull Seismol Soc Am, 100: 2866–2872
Zhu G, Wang Y, Liu G, Niu M, Xie C, Li C. 2005. $^{40}Ar/^{39}Ar$ dating of strike-slip motion on the Tan-Lu fault zone, East China. J Struct Geol, 27: 1379–1398
Zhu G, Liu G S, Niu M L, Xie C L, Wang Y S, Xiang B. 2009. Syn-collisional transform faulting of the Tan-Lu fault zone, East China. Int J Earth Sci-Geol Rundsch, 98: 135–155
Zhu G, Jiang D, Zhang B, Chen Y. 2012. Destruction of the eastern North China Craton in a backarc setting: Evidence from crustal deformation kinematics. Gondwana Res, 22: 86–103
Zhu R X, Fan H R, Li J W, Meng Q R, Li S R, Zeng Q D. 2015. Decratonic gold deposits. Sci China Earth Sci, 58: 1523–1537
Zhu R X, Yang J H, Wu F Y. 2012a. Timing of destruction of the North China Craton. Lithos, 149: 51–60
Zhu R X, Zhang H, Zhu G, Meng Q, Fan H, Yang J, Wu F, Zhang Z, Zheng T. 2017. Craton destruction and related resources. Int J Earth Sci-Geol Rundsch, 106: 2233–2257
Zhu R X, Zheng T Y. 2009. Destruction geodynamics of the North China craton and its Paleoproterozoic plate tectonics. Chin Sci Bull, 54: 3354–3366
Zhu R X, Xu Y G, Zhu G, Zhang H F, Xia Q K, Zheng T Y. 2012b. Destruction of the North China Craton. Sci China Earth Sci, 55: 1565–1587

(Responsible editor: Huajian YAO)